Chemical composition, genesis and exploration implication of garnet from the Hongshan Cu-Mo skarn deposit, SW China

Zhen-Dong Tian[a,c], Cheng-Biao Leng[a,b,*], Xing-Chun Zhang[a], Tehseen Zafar[a,c], Le-Jun Zhang[d], Wei Hong[d], Chun-Kit Lai[e]

[a] State Key Laboratory of Ore Deposit Geochemistry, Institute of Geochemistry, Chinese Academy of Sciences, Guiyang 550081, China
[b] State Key Laboratory of Nuclear Resources and Environment, East China University of Technology, Nanchang 330013, China
[c] University of Chinese Academy of Sciences, Beijing 100049, China
[d] Centre for Ore Deposit and Earth Sciences (CODES), University of Tasmania, Hobart 7001, Australia
[e] Faculty of Science, Universiti Brunei Darussalam, Gadong BE1410, Brunei

ARTICLE INFO

ABSTRACT

In this study, we present new mineral chemical data on the garnet from the Hongshan Cu-Mo deposit, one of the largest skarn deposits in the Sanjiang Tethyan tectonic domain, in SW China. The aims are to unravel the formation mechanism of the oscillatory-zoned garnet at Hongshan, and to explore possible applications using garnet trace element to distinguish different types of skarn deposits.

Two generations of garnets, i.e., poorly-zoned garnet I (Grt I) and the well-zoned garnet II (Grt II), are identified from the endoskarn and exoskarn, at Hongshan based on field and petrographic observations. EPMA and LA-ICP-MS analyses show that Grt I contains a narrow compositional range ($Adr_{40.07-61.25}$ $Grs_{36.65-57.08}$), and chondrite-normalized HREE-enriched and LREE-depleted patterns with minor positive Eu anomalies. In contrast, Grt II shows a wide compositional range ($Adr_{27.78-67.53}$ $Grs_{30.67-70.92}$ to almost pure andradite $Adr_{94.41-99.99}$ $Grs_{0.00-4.21}$) with interlayered Al-rich and Fe-rich zones. In Grt II, its Al-rich zone is chemically similar to Grt I, whereas its Fe-rich zone exhibits chondrite-normalized LREE-enriched and HREE-depleted patterns with distinct positive Eu anomalies. The positive REE^{3+} vs. Mg correlations, and the poor REE^{3+} vs. Y and Ca correlations, altogether indicate that the REE^{3+} incorporated into garnet was co-influenced by the menzerite-type substitution mechanism ($[Ca^{2+}]_{-1}^{VIII} [REE^{3+}]_{+1}^{VIII} [Al^{3+}]_{-1}^{VI} [Mg^{2+}]_{+1}^{VI}$), fluid chemistry, and the physicochemical conditions of precipitation. The higher U contents and HREE-enriched patterns of Grt I suggest that it was formed under a relatively reducing and near-neutral pH condition. Varying U contents and REE patterns across different oscillatory zones indicate that Grt II was probably formed under alternating physicochemical fluctuations led by repeating crack-seal cycles in the hydrothermal system. Besides, chemical data compilation suggests that the garnet from different types of skarn deposits has different compositions, and can be used as mineral prospecting tools. We suggested that discrimination plots, such as δEu vs. V and δCe vs. U, can distinguish Cu skarn deposit from other skarn deposit types, whilst the U vs. W plot can discriminate between Cu, W, W-Sn and W-Mo skarn deposits.

1. Introduction

Garnet is a common mineral in a wide range of igneous-metamorphic rock types, including mantle peridotites, metamorphic rocks, and peraluminous igneous rocks (e.g, Spengler et al., 2012; Baxter et al., 2013; Qian et al., 2013; Wood et al., 2013; Xu et al., 2013; Jollands et al., 2018). Garnet has been widely applied to estimate the temperature–pressure (P-T) conditions of mantle rocks, the P-T-t metamorphic history of metamorphic rocks based on the temperature-

dependent (e.g., Fe, Mg) and pressure-sensitive (e.g., Ca) elements exchange experiments between garnet and coexisting mineral phases (Caddick and Kohn, 2013; Qian et al., 2013; Beyer et al., 2015; Sun and Liang, 2015), and to date the metamorphic/mineralization events owing to its high Sm/Nd and Lu/Hf ratios (Blichert-Toft and Frei, 2001; Baxter and Scherer, 2013; Shu et al., 2013; Smit et al., 2013; Cheng et al., 2018). Hydrothermal garnets recorded the process of fluid-rock interactions and can therefore reveal the physicochemical conditions of hydrothermal mineralization, which include the fluid temperature,

---
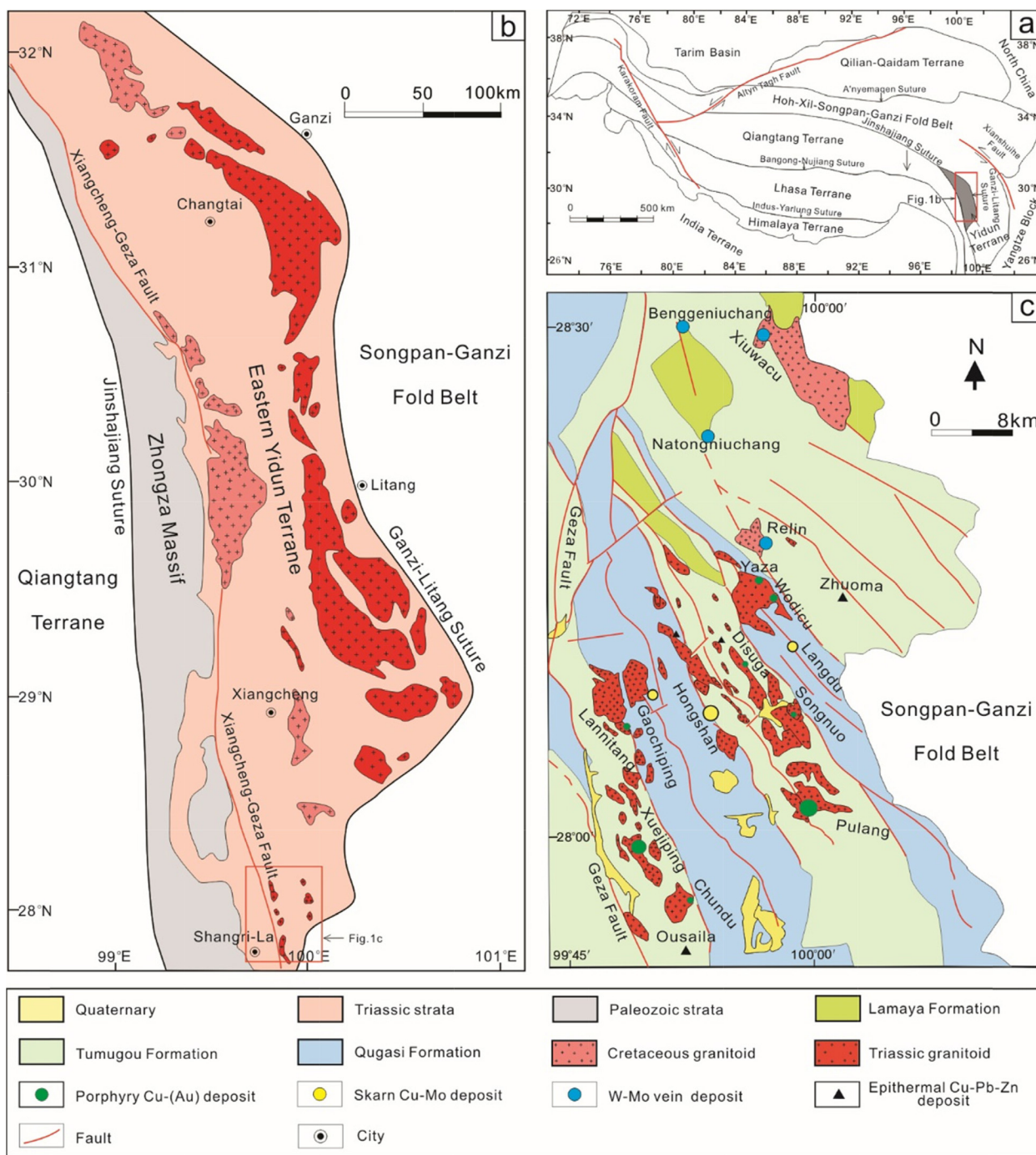
Fig. 1. (a) Location of the Yidun terrane in Tibetan Plateau. (b) Simplified geologic map of the Yidun terrane (modified after Wang et al., 2011a). (c) Geologic map of the southern Yidun terrane (modified after Leng et al., 2012).

oxygen fugacity, fluid flow rate, pH, and chemical compositions (Jamtveit et al., 1993; Gaspar et al., 2008; Zhai et al., 2014; Park et al., 2017b; Xiao et al., 2018). Over the past decade, many studies have been performed using garnet geochemical composition, U-Pb geochronology, and fluid inclusion temperature measurement to unravel the substitution mechanism of trace element into garnet, ore-forming age, and hydrothermal fluid evolution process during garnet growth (Smith et al., 2004; Zhai et al., 2014; Peng et al., 2015; Park et al., 2017b; Zhang et al., 2017a; Fu et al., 2018; Xiao et al., 2018). However, the formation mechanism of oscillatory zoning in hydrothermal garnet remains in debate (Jamtveit et al., 1993; Crowe et al., 2001). Some studies interpreted the oscillatory zoning as a result of episodic changes of

physiochemical conditions, while others favor a geochemically self-organizing mechanism (Yardley et al., 1991; Shore and Fowler, 1996; Pollok et al., 2001; Kohn, 2004).

In addition, the relationships between garnet geochemistry and skarn deposits varieties are not to be well established yet. Meinert (1992) proposed that garnets from different types of skarn deposits include various major element compositions, and established a series of discriminate diagrams for that. These discriminant diagrams, however, have significant overlaps in different types of skarn deposit, which limits its further usage in skarn deposit classification and mineral exploration. More recently, some workers suggested that garnets from Cu-dominated skarns have higher Cu contents than those from other types

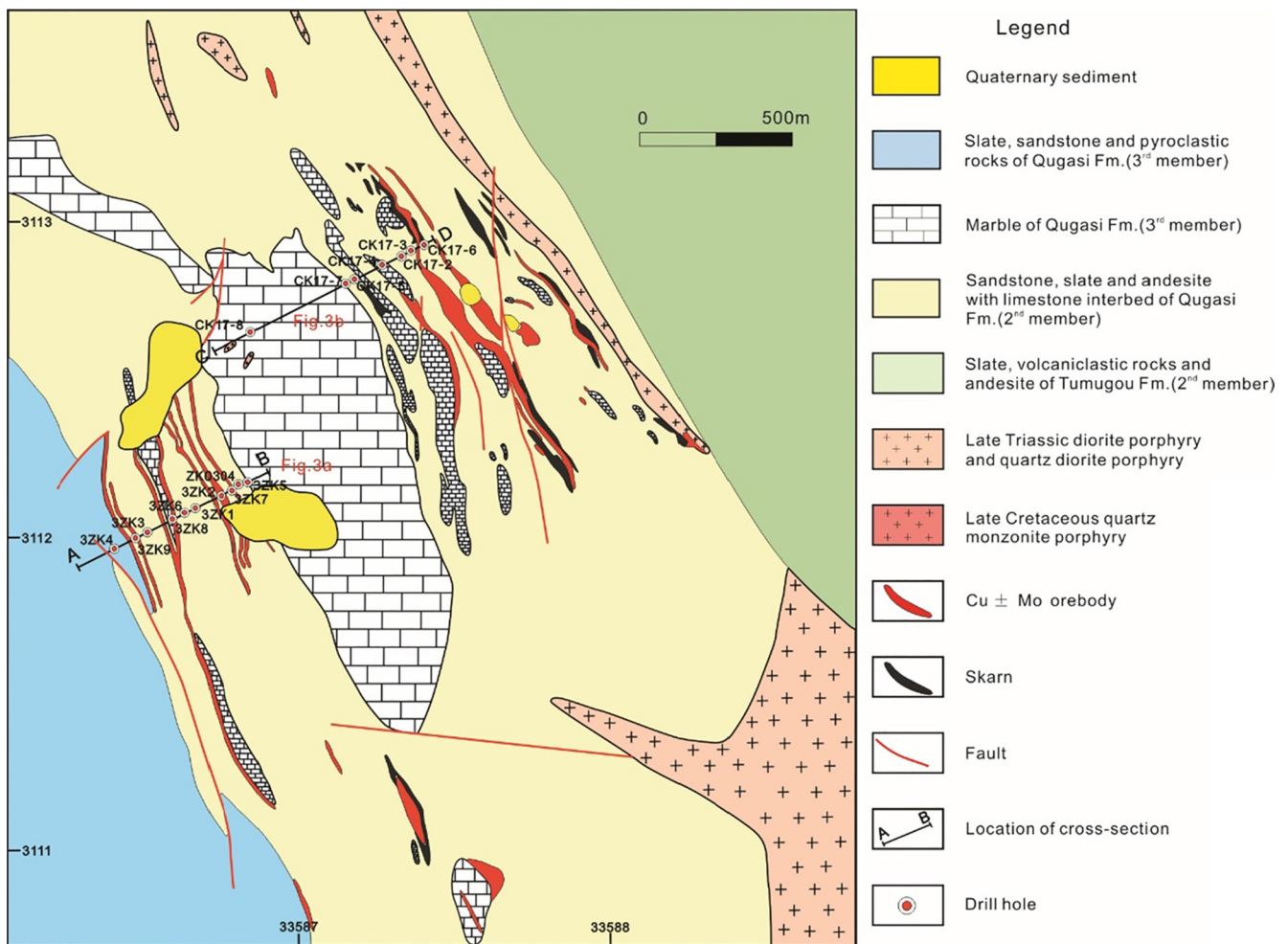**Fig. 2.** Geologic map of the Hongshan Cu-Mo skarn deposit (modified after Wang et al., 2014).

of skarns (Karimzadeh Somarin, 2004), and W-Sn skarns have high Sn content in their garnets (Zhou et al., 2017). These studies provide new insights into using garnet trace element chemistry to classify skarn deposits and mineral exploration.

The Hongshan Cu-Mo polymetallic deposit, located in the southeastern margin of the Tibetan Plateau, is one of the largest Cu skarn deposits in the Sanjiang Tethyan tectonic domain (Fig. 1). Previous studies on the skarn deposits at Hongshan were mainly dedicated to geological descriptions, mineralization ages, chemistry (including isotopes) of the ores and the ore-related intrusions (Xu et al., 2006; Li et al., 2013; Meng et al., 2013; Peng et al., 2014b; Wang et al., 2014, 2017b; Zu et al., 2015, 2016; Leng, 2017). Few studies have been done about its skarn minerals, such as garnet. Garnets from Hongshan are unusual in that it develops prominent oscillatory zoning, which provides us an excellent opportunity to unravel the origin of oscillatory zoning. Peng et al. (2015) presented the garnet chemical compositions, hydrogen-oxygen isotopes, and fluid inclusion data, and discussed the possible ways of trace element into garnet, garnet-forming fluid source, and formation environment (e.g., temperature and depth) of garnet. Nevertheless, comprehensive discussion on the mechanism (s) for trace-element substitution and oscillatory-zoning formation of the Hongshan garnets are scarce. In this study, we conducted integrated major and trace element analyses on different growth zones of two generations of garnets, and compiled published trace element data of garnet from different skarn deposits to discuss (1) REE substitution mechanism and formation environment of garnet, (2) formation of oscillatory zoning in garnet, (3) correlations between garnet trace element chemistry and different types of skarn deposits.

2. Geological background

Yidun terrane is situated in the southeastern margin of the Tibetan Plateau (Fig. 1a), and is separated from the Songpan-Ganzi fold belt by the Ganzi-Litang suture to the east, and from the Qiangtang terrane by the Jinshajiang suture to the west (Fig. 1b) (Reid et al., 2005a). The terrane can be further divided into two parts by the NNW-trending Xiangcheng-Geza fault (Fig. 1b). The Zhangza massif in the west consists of Paleozoic sedimentary rocks with minor mafic-intermediate volcanic rock interbeds (Reid et al., 2005a; Leng et al., 2014). These rocks have been metamorphosed to greenschist-amphibolite facies in Early Triassic due to the closure of Paleo-Tethys (Jinshajiang section) (Reid et al., 2005a,b). The Yidun terrane in the east is composed of the Middle to Upper Triassic flysch and mafic to felsic volcanic rocks, which were interpreted to have formed by the Late Triassic west-dipping subduction of the Paleo-Tethys (Ganzi-Litang section) (Leng et al., 2014).

Late Triassic intrusions in the northern Yidun terrane are extensively distributed along a N-S trending belt, parallel to the Ganzi-Litang suture zone (Fig. 1). These intrusions were emplaced during 237–207 Ma (magmatic peak at 216 Ma) (Wu et al., 2017). Extrusive rocks in the region comprise mainly bimodal volcanic rocks that host medium to large Pb-Zn-Ag VMS deposits, including the Gacun (Hou et al., 2001). Late Triassic magmatic rocks (230–206 Ma) in the southern Yidun terrane are composed of intermediate-felsic volcanic rocks, granitoids and porphyries, which are mostly characterized by high Sr/Y and La/Yb ratios, comparable to typical adakites (Leng et al., 2014; Cao et al., 2016). Many porphyry-type or skarn-type Cu-(Au)
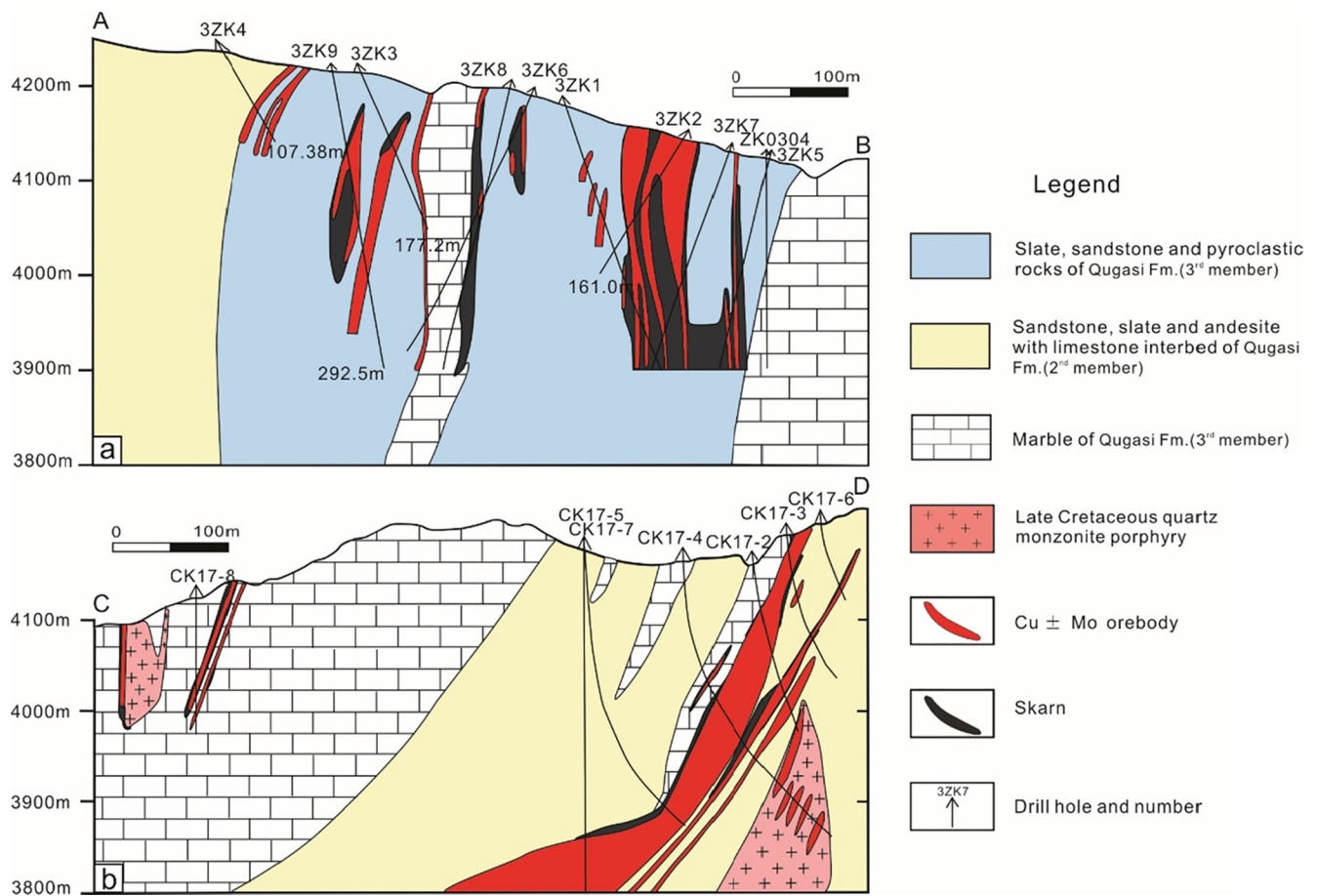
Fig. 3. Geologic cross sections of the Hongshan Cu-Mo skarn deposit, showing the spatial distribution of orebodies, sedimentary-volcanic sequences, and ore-causative intrusions. Location of the cross sections are shown in Fig. 2 (modified after Wang et al., 2014).

deposits, such as Pulang, Xuejiping, Lannitang and Langdu deposits (Fig. 1c), are spatially and genetically associated with these intrusions (Leng et al., 2012; Peng et al., 2014b; Li et al., 2017; Yang et al., 2017)

The Late Cretaceous granitoids (88–80 Ma) are emplaced along a N-S trending fault in the Yidun terrane (Li et al., 2017). These intrusions are characterized by high SiO$_2$, and K$_2$O + Na$_2$O contents, large ion lithophile elements (LILE) enrichments and high field strength element (HFSE) depletions, with varying negative ε$_{Hf(t)}$ (−9.5 to −2.3) and ε$_{Nd(t)}$ (−8.0 to −6.9), indicating that they were generated by partial melting of the ancient lower continental crust (Wang et al., 2014; Li et al., 2017). A series of porphyry- and skarn-type Cu-Mo deposits (e.g., Hongshan, Tongchanggou, and Xiuwacu) are genetically related to the Late Cretaceous granitoids (Fig. 1c) (Wang et al., 2014, 2017b; Li et al., 2017; Yang et al., 2017).

3. Ore deposit geology

The Hongshan Cu-Mo skarn deposit is situated at ~35 km northeast of the Shangri-La County, and is one of the largest Cu skarn deposits in southern Yidun terrane (Wang et al., 2014, 2017b; Zu et al., 2015). The Hongshan deposit consists of Hongshan, Hongniu and Enka ore blocks (Peng et al., 2014b), and contains a total reserve of 0.65 Mt Cu, 5769 t Mo, 323 t Ag, 7532 t WO$_3$, 6622 t Bi and 25262 t (Pb + Zn), respectively (Wang et al., 2014). Local exposed sequence includes the Upper Triassic Qugasi and Tumugou formations (Fig. 2), with the orebodies mainly confined within the former. The Hongshan ore block is hosted in the slate, limestone and siliceous rocks, whilst the Enka ore block is hosted in the clastic rocks, slate and limestone (Fig. 3) (Zu et al., 2015).

In the Hongshan district, two phases of intrusions have been

identified. The Late Triassic intrusions (224–216 Ma) occur as offshoots or dikes in northeastern Hongshan (Fig. 2) (Peng et al., 2014b). Age and geochemical studies suggested that these intrusions are genetically associated with the subduction of Ganzi-Litang Ocean in Late Triassic (Zu et al., 2015). The Late Cretaceous quartz monzonite porphyry and granite porphyry are found in middle Hongshan and drill holes, respectively. These intrusions were formed from 81 to 76 Ma (Wang et al., 2011b, 2014; Zu et al., 2015, 2016). Geochemically, these intrusions are characterized by high SiO$_2$ contents, and high Sr/Y and La/Yb ratios, comparable to those of typical adakites (Peng et al., 2014b; Wang et al., 2014). Moreover, most of the intrusions are subjected to slight to intense alteration (Wang et al., 2014; Zu et al., 2015, 2016).

Over 20 orebodies have been delineated at Hongshan, and generally occur in layered, stratoid, lenticular or veined forms (Figs. 2 and 3) (Zu et al., 2015; Wang et al., 2017a). These orebodies are hosted in skarn and hornfels zones (Peng et al., 2015), and are subparallel to the main NNW-striking structure (Figs. 2 and 3). The orebodies are 20–1223 m long, and 20 to 420 m wide (Zu et al., 2015). The deposit is characterized by Cu skarn mineralization in the shallow level and Mo porphyry mineralization at depth (Wang et al., 2014).

Based on mineral assemblages and ore texture, the alteration and mineralization can be divided into the prograde skarn (I), retrograde alteration (II), and quartz-sulfide mineralization (III) stages (Peng et al., 2015; Zu et al., 2016). At stage I, the intrusion emplacement caused the contact metamorphic/metasomatism of fine sandstone and carbonates into hornfels (albite-sericite-quartz-andalusite) and calc-silicate skarn (garnet-diopside-wollastonite- vesuvianite), respectively. Skarns at Hongshan can be further divided into endoskarn and exoskarn. The former is usually developed in a small scale along the margin of the
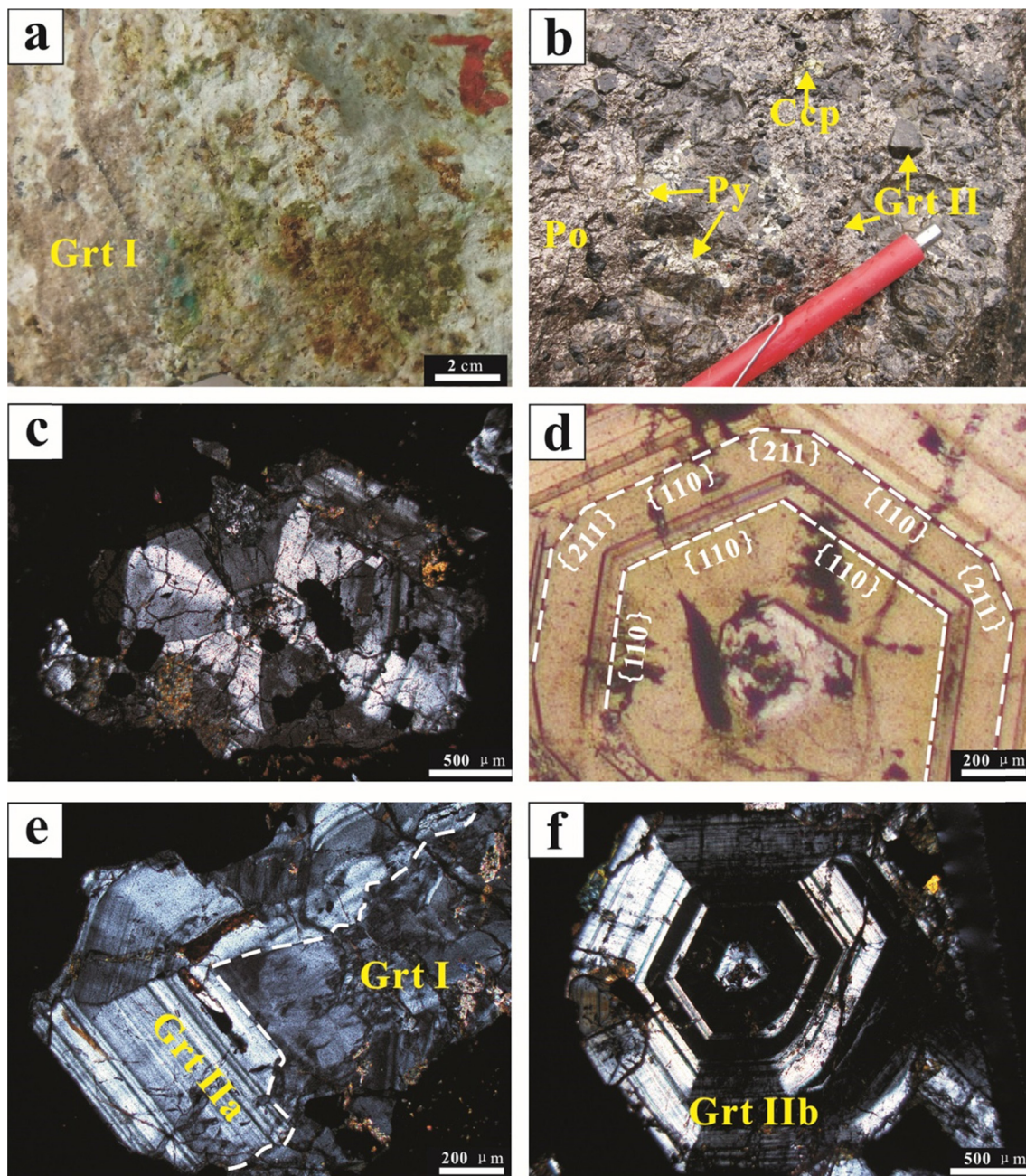
Fig. 4. Hand-specimen photos and thin-section microphotographs from the Hongshan Cu-Mo skarn deposit. (a) Grt I in endoskarn. (b) Euhedral and subhedral Grt II with interstitial pyrrhotite and chalcopyrite. (c) Subhedral Grt I with sector twinning and strong alteration on its grain margin. (d) Euhedral well-zoned Grt II, showing morphological transition from simple dodecahedral {1 1 0} in the core to composite dodecahedral {1 1 0}-trapezohedron {2 1 1} toward the margin. (e) Poorly-zoned Grt I with well-zoned Grt II overgrowth and an irregular boundary between them. (f) Well-zoned Grt II, with the dark and bright areas being FeO-rich and Al_2O_3-rich, respectively. Abbreviations: Ccp- chalcopyrite, Grt-garnet, Po-pyrrhotite, Py-pyrite.

quartz monzonite porphyry, with a mineral assemblage of garnet, diopside, and vesuvianite. The latter is widely developed in the mining area, and has a mineral assemblage of garnet, diopside, and wollastonite. Stage II is characterized with the replacement of the earlier anhydrous skarn minerals (e.g., garnet, diopside) by hydrous minerals (e.g., actinolite, epidote, tremolite) and sulfide precipitation (e.g., chalcopyrite, pyrite, pyrrhotite) to form massive and disseminate ores (Fig. 4a and b). In addition, massive and disseminated magnetite mineralization also occurred in this stage and frequently replaced garnet. Stage III is featured by quartz-sulfide (chalcopyrite-pyrite-pyrrhotite) veining.

At Hongshan, garnet is the most abundant skarn mineral and widely develops in both endoskarn and exoskarn (Peng et al., 2015). Detailed field investigations revealed that the garnet color and grain size vary significantly with increasing distance from the quartz monzonite porphyry (Peng et al., 2015). Two generations of garnets, i.e., garnet I (Grt I) and garnet II (Grt II), are identified (Fig. 4). Most of Grt I is hosted in the endoskarn. It is pale red to orange, fine-grained (mostly < 2 mm), and dodecahedral, and is anisotropic with low birefringence and sector twinning (Fig. 4a and c). The development of twinning suggests that the growth of Grt I was slow (Gaspar et al., 2008). In contrast, Grt II is generally hosted in exoskarn. It is red to brown, coarse-grained (0.2 to 1 cm), anisotropic and often contains fluid inclusions (Fig. 4b, d–f) (Peng et al., 2015). Grt II grains can be further divided into two subtypes (Grt IIa and IIb): Grt IIa grows around Grt I and contains fine oscillatory zoning (Fig. 4e). Grt IIb is euhedral and anisotropic, and
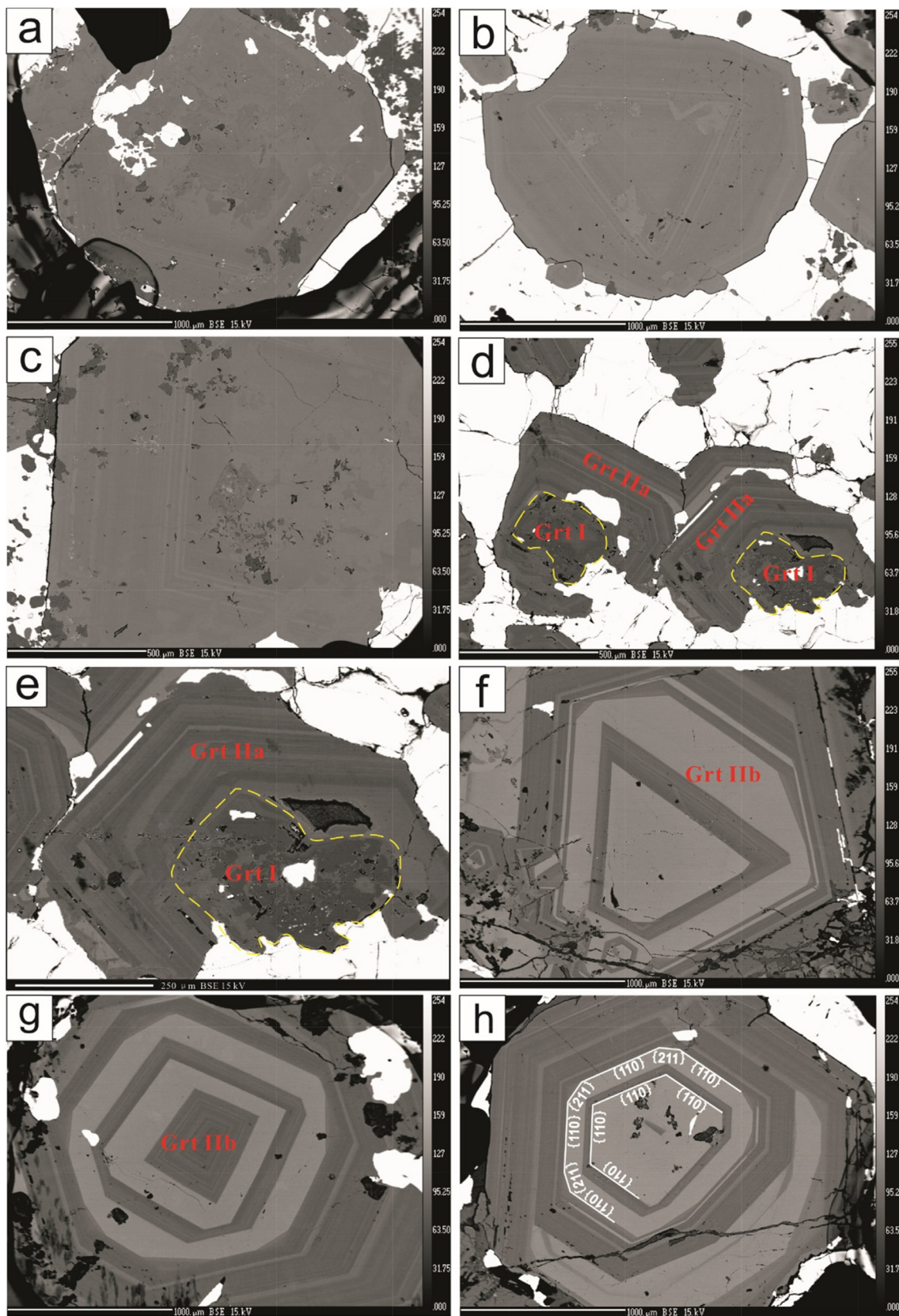
Fig. 5. BSE images of garnet from the Hongshan Cu-Mo skarn deposit. (a-c) Subhedral to anhedral poorly-zoned Grt I replaced by pyrrhotite. Resorbed garnet corners reflect resorption-corrosion process. (d-e) Well-zoned Grt II epitaxial overgrowth on poorly-zoned Grt I. (f-h) Euhedral Grt II with clear oscillatory zoning. In general, the dark gray areas are grandite ($Adr_{39.41-55.42}Grs_{42.67-57.69}$), and the bright-gray areas are mainly andradite ($Adr_{94.41-99.99}Grs_{0.00-4.21}$) and minor grandite ($Adr_{52.32-67.53}Grs_{30.67-45.72}$).

Table 1
EPMA analysis results (wt. %) of garnet from Hongshan Cu polymetallic deposit.

Garnet type							Grt I					
Sample number	HS11-2-C1-1	HS11-2-C1-2	HS11-2-C1-3	HS11-2-C1-4	HS11-2-C2-1	HS11-2-C2-2	HS11-2-C3-1	HS11-2-C4-1	HS11-2-C4-2	HS11-2-C4-3	HS11-2-C5-1	HS11-2-C5-2	HS11-2-C5-3
Description	dark gray	dark gray	dark gray	slightly bright gray	dark gray	slightly bright gray	dark gray	dark gray	slightly bright gray	dark gray	dark gray	dark gray	dark gray
SiO_2	35.08	35.84	35.57	35.84	35.79	36.02	35.45	35.41	34.42	35.16	35.14	35.19	36.55
TiO_2	1.76	2.27	2.28	0.79	2.06	1.77	1.56	2.06	2.63	2.33	2.16	1.53	2.14
Al_2O_3	9.10	11.30	11.14	6.97	10.81	8.03	9.32	9.03	7.51	10.73	10.21	9.11	10.29
FeO	16.58	13.45	13.75	19.90	14.33	17.32	16.52	15.98	17.43	14.09	14.61	16.63	14.69
MnO	0.58	0.69	0.68	0.49	0.63	0.51	0.61	0.61	0.48	0.65	0.59	0.63	0.63
MgO	0.18	0.24	0.23	0.17	0.21	0.16	0.17	0.16	0.29	0.23	0.20	0.17	0.27
CaO	33.77	33.77	33.60	33.44	33.70	34.26	33.69	33.44	32.99	33.48	33.92	33.79	34.33
Na_2O	0.00	0.02	0.00	0.03	0.00	0.02	0.04	0.02	0.01	0.00	0.00	0.01	0.00
K_2O	0.01	0.01	0.00	0.00	0.01	0.00	0.01	0.00	0.00	0.00	0.00	0.00	0.00
Total	97.05	97.58	97.24	97.64	97.53	98.09	97.38	96.70	95.76	96.68	96.84	97.06	98.90
Si	2.90	2.91	2.90	2.97	2.91	2.95	2.92	2.93	2.89	2.89	2.89	2.91	2.93
Al^{IV}	0.10	0.09	0.10	0.03	0.09	0.05	0.08	0.07	0.11	0.11	0.11	0.09	0.07
Al^{VI}	0.82	1.02	1.00	0.68	0.98	0.75	0.86	0.84	0.67	0.96	0.91	0.83	0.94
Ti	0.11	0.14	0.14	0.05	0.13	0.11	0.10	0.13	0.17	0.14	0.13	0.09	0.13
Fe^{3+}	0.92	0.72	0.74	1.08	0.76	0.97	0.90	0.88	0.99	0.77	0.82	0.92	0.80
Fe^{2+}	0.23	0.19	0.20	0.30	0.21	0.22	0.24	0.22	0.24	0.20	0.19	0.23	0.19
Mn	0.04	0.05	0.05	0.03	0.04	0.04	0.04	0.04	0.03	0.05	0.04	0.04	0.04
Mg	0.02	0.03	0.03	0.02	0.03	0.02	0.02	0.02	0.04	0.03	0.02	0.02	0.03
Ca	2.99	2.94	2.94	2.97	2.94	3.00	2.97	2.96	2.97	2.95	2.99	2.99	2.95
Almandine	0.00	0.00	0.00	0.00	0.00	0.00	0.00	0.00	0.00	0.00	0.00	0.00	0.00
Andradite	50.82	40.07	40.77	61.25	42.41	55.57	49.80	50.03	57.05	42.49	45.21	50.89	45.02
Grossular	46.89	57.08	56.49	36.65	55.05	42.32	47.83	47.61	40.25	54.78	52.34	46.71	52.14
Pyrope	0.81	1.09	1.02	0.80	0.94	0.75	0.78	0.75	1.38	1.06	0.92	0.76	1.21
Spessartine	1.49	1.75	1.72	1.30	1.60	1.36	1.59	1.61	1.32	1.66	1.53	1.64	1.62
Uvarovite	0.00	0.00	0.00	0.00	0.00	0.00	0.00	0.00	0.00	0.00	0.00	0.00	0.00

Garnet type	Grt II												
Sample number	HS11-1-C1-1	HS11-1-C1-2	HS11-1-C1-3	HS11-1-C1-4	HS11-1-C1-5	HS11-1-C1-6	HS11-1-C1-7	HS11-1-C1-8	HS11-1-C1-9	HS11-1-C1-10	HS11-1-C1-11	HS11-1-C1-12	HS11-1-C1-13
Description	dark gray	slightly bright gray	dark gray	slightly bright gray	dark gray	slightly bright gray	dark gray	bright gray	dark gray	bright gray	bright gray	slightly bright gray	bright gray
SiO_2	35.87	35.48	35.95	34.30	36.97	36.09	37.05	35.30	36.77	34.52	33.63	36.14	35.31
TiO_2	0.26	0.04	0.22	0.08	0.68	0.11	0.62	0.00	0.52	0.02	0.00	0.94	0.00
Al_2O_3	9.73	8.31	10.33	6.76	10.14	7.48	10.22	0.12	8.23	0.28	0.17	7.26	0.06
FeO	16.92	18.99	16.37	21.05	15.94	19.51	16.10	27.83	18.52	27.35	27.17	19.18	28.00
MnO	0.64	0.53	0.65	0.48	0.59	0.45	0.52	0.21	0.48	0.12	0.16	0.39	0.18
MgO	0.11	0.08	0.12	0.10	0.16	0.10	0.13	0.11	0.15	0.22	0.24	0.20	0.12
CaO	33.67	33.49	33.89	32.97	34.28	33.68	34.24	33.21	34.00	33.27	32.49	34.07	33.09
Na_2O	0.00	0.01	0.00	0.01	0.00	0.00	0.00	0.01	0.02	0.03	0.03	0.01	0.03
K_2O	0.00	0.00	0.00	0.00	0.00	0.00	0.01	0.00	0.00	0.00	0.01	0.00	0.00
Total	97.19	96.93	97.53	95.73	98.76	97.43	98.90	96.78	98.69	95.82	93.90	98.19	96.80
Si	2.95	2.95	2.94	2.92	2.98	2.99	2.98	3.04	2.99	3.00	2.99	2.97	3.04
Al^{IV}	0.05	0.05	0.06	0.08	0.02	0.01	0.02	0.00	0.01	0.00	0.01	0.03	0.00
Al^{VI}	0.94	0.80	0.98	0.63	0.98	0.75	0.99	0.01	0.82	0.03	0.01	0.70	0.01
Ti	0.02	0.00	0.01	0.01	0.04	0.01	0.04	0.00	0.03	0.00	0.00	0.06	0.00
Cr	0.00	0.00	0.00	0.00	0.00	0.00	0.00	0.00	0.00	0.00	0.00	0.00	0.00
Fe^{3+}	0.90	1.02	0.86	1.16	0.84	1.05	0.84	1.61	0.98	1.63	1.65	1.05	1.62
Fe^{2+}	0.27	0.31	0.26	0.34	0.23	0.30	0.25	0.39	0.28	0.36	0.38	0.27	0.40
Mn	0.04	0.04	0.05	0.03	0.04	0.03	0.04	0.02	0.03	0.01	0.01	0.03	0.01
Mg	0.01	0.01	0.01	0.01	0.02	0.01	0.02	0.01	0.02	0.03	0.03	0.02	0.01
Ca	2.97	2.99	2.97	3.01	2.96	2.99	2.95	3.06	2.96	3.10	3.10	3.00	3.05
Total	8.15	8.16	8.15	8.19	8.11	8.15	8.11	8.15	8.12	8.17	8.18	8.13	8.15
Almandine	0.00	0.00	0.00	0.00	0.00	0.00	0.00	0.00	0.00	0.00	0.00	0.00	0.00
Andradite	48.74	55.49	46.42	63.02	46.61	59.05	46.30	99.26	55.42	98.25	98.92	59.96	99.60
Grossular	49.18	42.78	51.46	35.27	51.17	39.31	51.81	0.00	42.67	0.24	0.00	38.09	0.00
Pyrope	0.47	0.37	0.51	0.46	0.73	0.45	0.59	0.58	0.67	1.16	1.08	0.91	0.40
Spessartine	1.61	1.35	1.61	1.25	1.49	1.19	1.31	0.16	1.24	0.34	0.00	1.04	0.00
Uvarovite	0.00	0.00	0.00	0.00	0.00	0.00	0.00	0.00	0.00	0.00	0.00	0.00	0.00

Garnet type	Grt II												
Sample number	HS11-1-C1-14	HS11-1-C1-15	HS11-1-C1-16	HS11-1-C1-17	HS11-1-C1-18	HS11-1-C2-16	HS11-1-C2-17	HS11-1-C2-18	HS11-1-C2-19	HS11-1-C2-20	HS11-1-C2-21	HS11-1-C3-1	HS11-1-C3-2
Description	slightly bright gray	slightly bright gray	dark gray	bright gray	slightly bright gray	bright gray	dark gray	bright gray	dark gray	slightly bright gray	dark gray	dark gray	bright gray
SiO_2	36.21	34.99	36.00	34.76	36.79	35.07	36.53	34.92	36.86	35.47	36.70	37.07	35.22
TiO_2	0.13	0.11	0.19	0.00	0.02	0.00	1.13	0.01	0.87	0.04	0.25	0.27	0.02
Al_2O_3	7.87	6.87	9.41	0.37	9.03	0.11	9.67	0.07	11.31	7.10	9.64	10.47	0.92
FeO	18.99	20.38	17.32	27.79	18.06	27.72	16.02	28.04	14.67	19.96	17.25	16.39	27.73
MnO	0.49	0.48	0.57	0.26	0.64	0.19	0.52	0.24	0.67	0.40	0.62	0.60	0.23

Table 1 (*continued*)

MgO	0.11	0.12	0.13	0.13	0.08	0.12	0.17	0.10	0.19	0.11	0.14	0.12	0.14
CaO	34.12	33.40	33.71	32.77	34.14	32.93	34.27	33.03	34.22	33.85	33.91	34.09	33.03
Na$_2$O	0.00	0.01	0.00	0.00	0.00	0.00	0.01	0.00	0.01	0.01	0.00	0.00	0.00
K$_2$O	0.00	0.00	0.01	0.00	0.00	0.00	0.00	0.00	0.00	0.00	0.00	0.01	0.01
Total	97.92	96.36	97.33	96.07	98.76	96.15	98.32	96.41	98.80	96.94	98.51	99.03	97.29
Si	2.98	2.95	2.96	3.02	2.99	3.04	2.96	3.02	2.96	2.96	2.98	2.98	3.01
Al ^{IV}	0.02	0.05	0.04	0.00	0.01	0.00	0.04	0.00	0.04	0.04	0.02	0.02	0.00
Al ^{VI}	0.78	0.66	0.91	0.04	0.89	0.01	0.92	0.01	1.06	0.70	0.94	1.01	0.10
Ti	0.01	0.01	0.01	0.00	0.00	0.00	0.07	0.00	0.05	0.00	0.02	0.02	0.00
Cr	0.00	0.00	0.00	0.00	0.00	0.00	0.00	0.00	0.00	0.00	0.00	0.00	0.00
Fe^{3+}	1.03	1.13	0.92	1.61	0.95	1.61	0.86	1.63	0.76	1.10	0.90	0.84	1.57
Fe^{2+}	0.27	0.31	0.27	0.41	0.28	0.40	0.22	0.40	0.22	0.29	0.27	0.27	0.42
Mn	0.03	0.03	0.04	0.02	0.04	0.01	0.04	0.02	0.05	0.03	0.04	0.04	0.02
Mg	0.01	0.01	0.02	0.02	0.01	0.02	0.02	0.01	0.02	0.01	0.02	0.01	0.02
Ca	3.01	3.02	2.97	3.05	2.97	3.06	2.98	3.06	2.94	3.03	2.95	2.94	3.03
Total	8.15	8.17	8.14	8.16	8.14	8.15	8.11	8.16	8.11	8.17	8.13	8.12	8.16
Almandine	0.00	0.00	0.00	0.00	0.00	0.00	0.00	0.00	0.00	0.00	0.00	0.00	0.00
Andradite	57.53	62.31	50.20	97.73	52.32	99.28	48.36	99.54	41.58	61.22	49.29	45.68	94.41
Grossular	40.72	35.89	47.78	0.84	45.72	0.00	49.56	0.00	55.93	37.25	48.55	52.27	4.21
Pyrope	0.48	0.55	0.57	0.67	0.36	0.66	0.76	0.46	0.84	0.48	0.61	0.54	0.70
Spessartine	1.27	1.26	1.45	0.76	1.61	0.06	1.32	0.00	1.65	1.05	1.56	1.50	0.68
Uvarovite	0.00	0.00	0.00	0.00	0.00	0.00	0.00	0.00	0.00	0.00	0.00	0.00	0.00

Garnet type	Grt II												
Sample number	HS11-1-C3-3	HS11-1-C3-4	HS11-1-C3-5	HS11-1-C3-6	HS11-1-C3-7	HS11-1-C6-1	HS11-1-C6-2	HS11-1-C6-3	HS11-1-C6-4	HS11-1-C6-5	HS11-1-C6-6	HS11-1-C6-7	HS11-5-C2-1
Description	dark gray	bright gray	dark gray	bright gray	dark gray	slightly bright gray	dark gray	bright gray	slightly bright gray	bright gray	dark gray	dark gray	dark gray
SiO$_2$	36.34	34.81	36.26	34.53	36.02	35.23	36.53	34.74	35.99	34.43	36.13	36.49	35.00
TiO$_2$	0.45	0.00	0.77	0.00	0.31	0.01	0.62	0.00	1.09	0.00	0.57	1.52	0.05
Al$_2$O$_3$	9.99	0.05	9.67	0.15	15.28	5.86	10.88	0.00	8.69	0.11	9.93	11.54	11.81
FeO	16.81	27.92	16.88	27.56	9.85	21.50	15.18	27.98	17.32	27.55	15.77	13.16	12.91
MnO	0.59	0.23	0.53	0.12	0.32	0.44	0.55	0.22	0.51	0.14	0.25	0.62	0.26
MgO	0.15	0.12	0.22	0.19	0.13	0.14	0.16	0.12	0.21	0.20	0.12	0.30	0.09
CaO	33.94	33.00	33.73	33.07	35.47	33.81	34.21	32.85	33.80	32.98	34.86	34.12	37.48
Na$_2$O	0.01	0.01	0.00	0.01	0.00	0.00	0.00	0.00	0.00	0.00	0.01	0.00	0.03
K$_2$O	0.00	0.00	0.00	0.00	0.01	0.00	0.00	0.01	0.00	0.00	0.00	0.00	0.00
Total	98.29	96.13	98.06	95.62	97.39	96.97	98.13	95.94	97.60	95.42	97.62	97.76	97.64
Si	2.96	3.02	2.96	3.01	2.89	2.96	2.96	3.02	2.95	3.01	2.95	2.95	2.85
Al ^{IV}	0.04	0.00	0.04	0.00	0.11	0.04	0.04	0.00	0.05	0.00	0.05	0.05	0.15
Al ^{VI}	0.95	0.01	0.92	0.02	1.37	0.57	1.03	0.00	0.83	0.01	0.94	1.08	1.02
Ti	0.03	0.00	0.05	0.00	0.02	0.00	0.04	0.00	0.07	0.00	0.04	0.09	0.00
Cr	0.00	0.00	0.00	0.00	0.00	0.00	0.00	0.00	0.00	0.00	0.00	0.00	0.00
Fe^{3+}	0.88	1.63	0.88	1.63	0.54	1.21	0.80	1.63	0.94	1.64	0.88	0.71	0.84
Fe^{2+}	0.27	0.40	0.27	0.38	0.13	0.30	0.23	0.40	0.25	0.38	0.20	0.17	0.04
Mn	0.04	0.02	0.04	0.01	0.02	0.03	0.04	0.02	0.04	0.01	0.02	0.04	0.02
Mg	0.02	0.02	0.03	0.02	0.02	0.02	0.02	0.02	0.03	0.03	0.01	0.04	0.01
Ca	2.96	3.07	2.95	3.09	3.05	3.04	2.97	3.06	2.97	3.09	3.05	2.95	3.27
Total	8.14	8.16	8.13	8.16	8.13	8.18	8.12	8.16	8.12	8.17	8.13	8.09	8.20
Almandine	0.00	0.00	0.00	0.00	0.00	0.00	0.00	0.00	0.00	0.00	0.00	0.00	0.00
Andradite	47.82	99.69	48.75	99.08	27.78	67.53	43.51	99.99	52.79	99.34	47.85	39.41	44.24
Grossular	50.05	0.00	48.96	0.00	70.92	30.67	54.45	0.00	44.93	0.00	51.02	57.69	54.74
Pyrope	0.65	0.31	0.96	0.92	0.54	0.64	0.68	0.01	0.94	0.66	0.51	1.33	0.40
Spessartine	1.49	0.00	1.34	0.00	0.76	1.16	1.36	0.00	1.34	0.00	0.62	1.57	0.62
Uvarovite	0.00	0.00	0.00	0.00	0.00	0.00	0.00	0.00	0.00	0.00	0.00	0.00	0.00

Garnet type	Grt II							
Sample number	HS11-5-C2-2	HS11-5-C2-3	HS11-5-C2-4	HS11-5-C2-5	HS11-5-C2-6	HS11-5-C2-7	HS11-5-C2-8	HS11-5-C2-9
Description	slightly bright gray	dark gray	slightly bright gray	slightly bright gray	dark gray	bright gray	slightly bright gray	dark gray
SiO$_2$	34.86	35.63	34.24	34.56	35.31	33.51	35.34	35.28
TiO$_2$	0.64	0.63	0.03	0.02	0.07	0.00	0.02	0.35
Al$_2$O$_3$	7.08	10.79	6.20	6.20	10.55	0.29	8.23	9.95
FeO	17.99	14.04	19.83	19.78	14.94	27.11	17.66	15.15
MnO	0.18	0.61	0.39	0.46	0.64	0.26	0.56	0.65
MgO	0.11	0.16	0.13	0.07	0.11	0.14	0.10	0.13
CaO	36.81	36.41	35.50	35.61	35.99	34.74	35.80	36.25
Na$_2$O	0.01	0.00	0.00	0.01	0.04	0.00	0.00	0.00
K$_2$O	0.00	0.00	0.00	0.01	0.01	0.00	0.00	0.00
Total	97.67	98.29	96.32	96.71	97.66	96.07	97.71	97.78
Si	2.89	2.89	2.90	2.91	2.89	2.92	2.92	2.89
Al ^{IV}	0.11	0.11	0.10	0.09	0.11	0.03	0.08	0.11
Al ^{VI}	0.61	0.96	0.55	0.56	0.95	0.00	0.75	0.88
Ti	0.04	0.04	0.00	0.00	0.00	0.00	0.00	0.02
Cr	0.00	0.00	0.00	0.00	0.00	0.00	0.00	0.00
Fe^{3+}	1.14	0.86	1.23	1.22	0.90	1.69	1.06	0.94
Fe^{2+}	0.10	0.09	0.17	0.17	0.12	0.28	0.16	0.10
Mn	0.01	0.04	0.03	0.03	0.04	0.02	0.04	0.04

Table 1 (*continued*)

Mg	0.01	0.02	0.02	0.01	0.01	0.02	0.01	0.02
Ca	3.27	3.16	3.22	3.21	3.16	3.25	3.16	3.18
Total	8.19	8.17	8.21	8.20	8.19	8.22	8.19	8.18
Almandine	0.00	0.00	0.00	0.00	0.00	0.00	0.00	0.00
Andradite	62.34	45.63	66.54	66.47	46.95	98.26	57.03	49.41
Grossular	36.68	52.22	31.87	32.01	51.04	0.28	41.13	48.44
Pyrope	0.50	0.68	0.59	0.34	0.46	0.72	0.44	0.57
Spessartine	0.47	1.47	1.01	1.18	1.54	0.74	1.40	1.58
Uvarovite	0.00	0.00	0.00	0.00	0.00	0.00	0.00	0.00

Note: All the calculations are based on 12 oxygens.
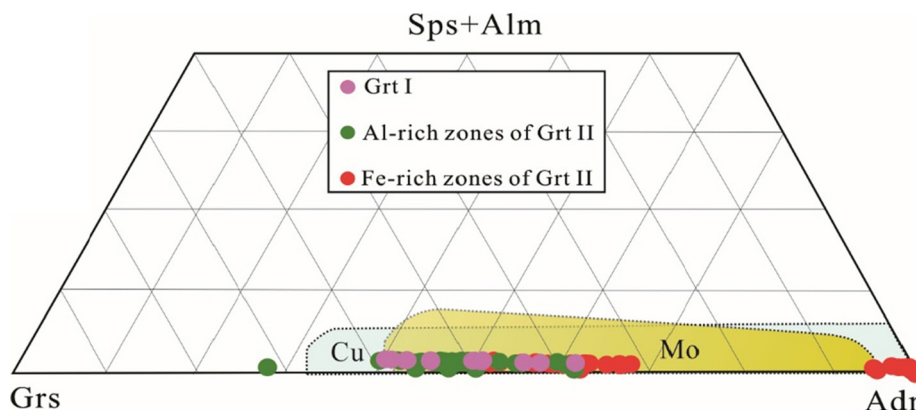
Fig. 6. Classification diagram of garnet in the Hongshan Cu-Mo skarn deposit, with comparison to the garnet from Cu and Mo skarn deposits worldwide (the Cu and Mo skarn fields from Meinert et al., 2005). Abbreviations: Sps-spessartine, Alm-almandine, Grs-grossular, Adr-andradite.

shows clearly coarse oscillatory zoning and development of trapezo-hedron {2 1 1} faces (Fig. 4d and f). This indicates that the growth of Grt IIb was rapid (Jamtveit et al., 1993).

4. Analytical methods

4.1. EPMA

Prior to the Electron Probe Microanalysis (EPMA), ten typical garnet-bearing ore samples from different skarn zones (in both en-doskarn and exoskarn) were mounted and polished in epoxy resin. A total of 60 EPMA spot analyses have been conducted. Backscattered electron (BSE) imaging on representative garnet grains were conducted with a FEI Quanta 600 environmental SEM in the Central Science Laboratory (CSL) at the University of Tasmania (UTAS). Compositional data were acquired on a Cameca SX100 EPMA equipped with five tunable wavelength dispersive spectrometers in the same laboratory. Analysis conditions include 10 nA beam current, 15 kV voltage and 2–5 μm beam size. The counting time was 10 s for Na, Si, K, 15 s for Ca, and 20 s for Mg, Ti, Al, Mn, Fe. The analyses were calibrated using hematite (Fe), bustamite (Mn), rutile (Ti), microcline (K), clinopyr-oxene (Si, Ca), plagioclase (Al), olivine (Mg), and anorthoclase (Na) standards. The detection limits for most elements are 0.01 wt%. The precisions are < 1% for element concentrations above 10 wt%, < 5% for element concentrations between 1 and 10 wt%, and > 5% for element concentrations below 1 wt%.

4.2. LA-ICP-MS

After petrographic and EPMA analyses, nine representative samples were selected for Laser Ablation-Inductively Coupled Plasma-Mass spectrometry (LA-ICP-MS) trace element analysis. To avoid the influ-ence of mineral inclusions, micro-fractures and overlapping oscillatory zones in garnet, each analysis spot was carefully selected via trans-mitted light microscopy and BSE images. A total of 46 LA-ICP-MS spot analyses were conducted, among which 41 spots yielded

uncontaminated meaningful results. The analysis was performed at the Centre for Ore Deposits and Earth Sciences (CODES, UTAS), using an Agilent 7500cs ICP-MS coupled with a 193 nm ArF excimer Resonetics RESOlution S-155 laser-ablation system. Helium and argon were used as the carrier gas and make-up gas, respectively. Analytical conditions include 32 μm spot size, 10 Hz frequency and 3.58 J/cm^2 energy den-sity. The NIST 612 and GSD-1 g standard glass were analyzed once every 10 analyses as the external standard, while Ca^{44} was used for the internal standard. The raw data were exported from the ICP-MS and processed using the Sills software. Detection limits for most trace ele-ments were of 0.01 to 0.5 ppm.

5. Results

5.1. Garnet petrography

In BSE images, most Grt I grains are subhedral to anhedral granular, dark gray, varying in sizes (0.7–2 mm), and with poor compositional zoning and irregular boundaries (Fig. 5a–c). Surrounding minerals in-clude pyrrhotite, chalcopyrite, pyrite, magnetite, epidote and chlorite. The fine oscillatory-zoned Grt IIa is subhedral and overgrows on Grt I (Fig. 5d-e). Grt IIb is mostly euhedral (size: 0.2–1 mm) (Fig. 5f–h), and is featured by distinct coarse oscillatory zoning with local morpholo-gical transition from simple dodecahedral {1 1 0} to composite dode-cahedral {1 1 0}-trapezohedral {2 1 1}.

5.2. Major element compositions

Major element compositions of two generation of garnet are given in Table 1. The results show that these garnets belong to grossular-an-dradite (grandite) solid solution. Other end member components, such as almandine, spessartine, pyrope and uvarovite, are < 3%. Grt I has poor compositional zoning and falls within a relative narrow compo-sitional range of $Adr_{40.07-61.25}Grs_{36.65-57.08}Sps_{1.30-1.75}Pyr_{0.75-1.38}$ (Fig. 6). The concentrations of SiO_2, Al_2O_3, CaO, FeO are 34.42–36.55 wt%, 6.97–11.30 wt%, 32.99–34.33 wt% and
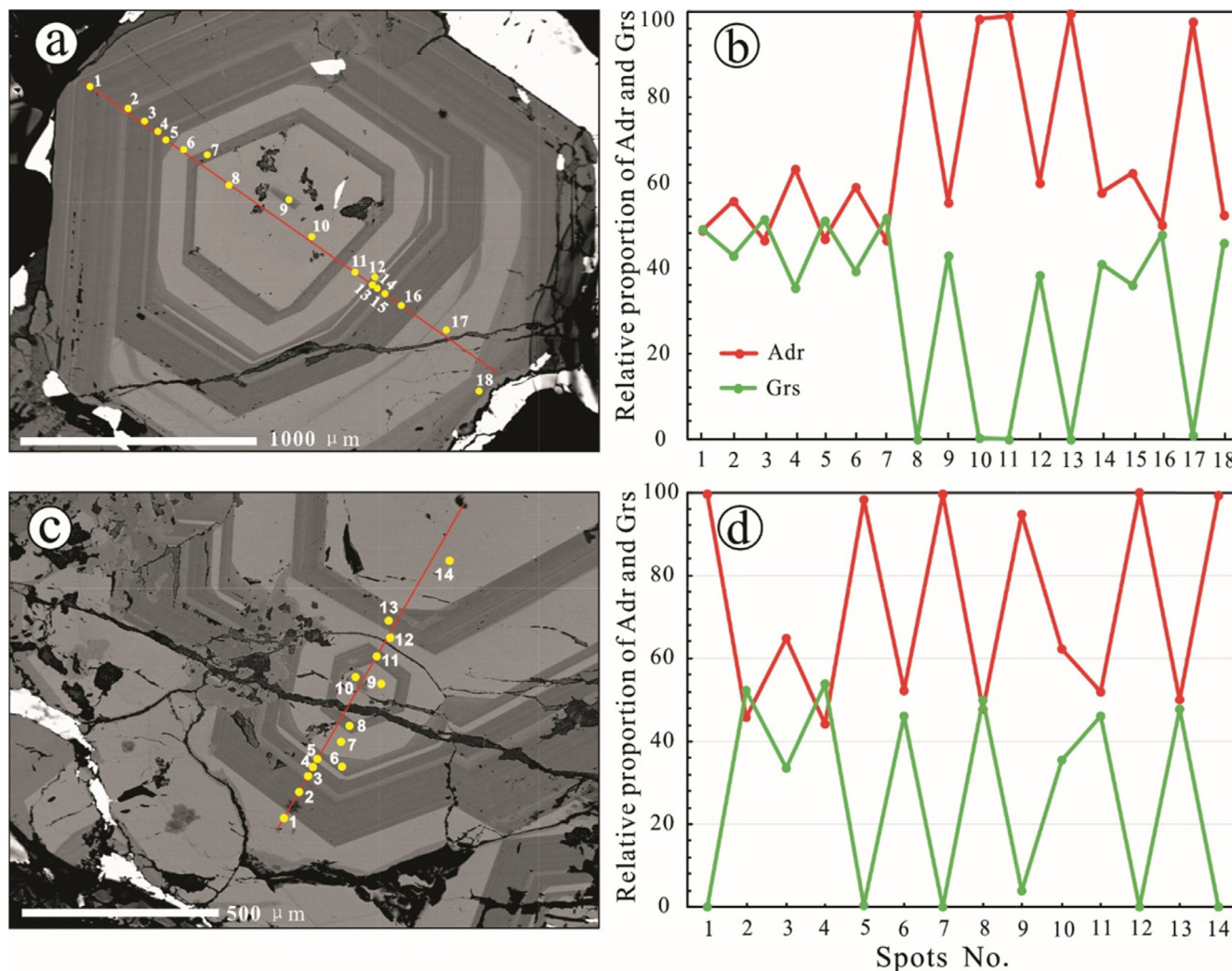
Fig. 7. BSE images (left) and compositional variation profiles of the Garnet II at Hongshan. Yellow dots and white numbers represent the EPMA locations and spot numbers, respectively. Abbreviations: Adr-andradite, Grs-grossular. (For interpretation of the references to color in this figure legend, the reader is referred to the web version of this article.)

13.45–19.90 wt%, respectively (Table 1).

In general, the brighter area in BSE images is more andraditic than darker area (Fig. 7). The dark-gray (Al-rich) zones have SiO_2, Al_2O_3, CaO, and FeO contents of 35.00–37.07 wt%, 8.23–15.28 wt%, 33.67–37.48 wt%, and 9.85–18.52 wt%, respectively. In addition, the Grt II Al-rich zones have nearly equal end member compositions of andradite and grossular, and mostly fall within a compositional range $(Adr_{39.41-55.42} Grs_{42.67-57.69}Sps_{0.62-1.65}Pyr_{0.40-1.33})$ similar to the Grt I (Fig. 6). The bright-gray (Fe-rich) zones have 33.51–36.79 wt% SiO_2, 0.00–9.03 wt% Al_2O_3, 32.49–36.81 wt% CaO, and 17.32–28.04 wt% FeO. They have a wide compositional range from $Adr_{52.32-67.53}Grs_{30.67-45.72} Sps_{0.47-1.61}Pyr_{0.34-0.94}$ to almost pure andradite $(Adr_{94.41-99.99}Grs_{0.00-4.21} Sps_{0.00-0.76}Pyr_{0.01-1.16})$ (Figs. 6 and 7). The Grt II Fe-rich zones have generally lower Al_2O_3 but higher FeO contents than the Grt I and Grt II Al-rich zones.

5.3. Trace element compositions

The LA-ICP-MS results of two generations of garnet are listed in Table 2. The results show that all the garnets analyzed are depleted in large ion lithophile elements (LILEs, e.g., K, Sr) relative to the primitive mantle (Sun and McDonough, 1989) (Fig. 8a; Table 2). High field strength elements (HFSE, e.g., Ti, Zr, Hf) are enriched in most of Grt I and Grt II Al-rich zones and depleted in Grt II Fe-rich zones relative to

primitive mantle (Fig. 8b-d). In addition, the total HFSE contents (sum of Ti, Zr and Hf contents) decrease from Grt I (9209–13,312 ppm, mean 11,957 ppm), to Grt II Al-rich zone (771–7071 ppm, mean 3336 ppm), to Grt II Fe-rich zone (mostly < 20 ppm, mean = 16.9 ppm). Concentrations of Mn, Sc, V, Cr, U, and Y decrease from Grt I to Grt II Al-rich zones to Grt II Fe-rich zones (Table 2). For instance, Grt I generally contains the highest U (15.5–37.9 ppm, mean = 22.5 ppm), while the Fe-rich zones Grt II have the lowest U (1.77 to 10.9 ppm, mean = 4.93 ppm) (Fig. 8f). Contents of other trace elements (e.g., Th and W) are highest in Grt II Al-rich zones (Fig. 8e), whereas Fe content is highest in Grt II Fe-rich zones.

In general, the Grt I and Grt II Al-rich zones display similar REE patterns with strong heavy rare earth elements (HREE) enrichment and light rare earth elements (LREE) depletion, and minor (positive or negative) Eu anomalies (Fig. 9). The Grt II Al-rich zones have higher total REE (ΣREE = 60.4 − 182 ppm, mean 113 ppm), and LREE (37.3 − 93.6 ppm, mean 55.3 ppm) contents, and LREE/HREE ratios (0.30 − 2.16, mean 1.16) than Grt I (ΣREE = 60.6 − 246 ppm, mean = 110 ppm; ΣLREE = 14.8 − 37.8 ppm, mean = 24.6 ppm; LREE/HREE = 0.13 − 0.71, mean = 0.39). The Grt II Fe-rich zones (except one data of HS11-1-C6-01) generally have much lower ΣREE (11.7 − 41.5 ppm, mean 24.7 ppm), LREE (11.0 − 38.6 ppm, mean 23.3 ppm), and HREE (0.14 − 4.03 ppm, mean 1.46 ppm), but much higher LREE/HREE ratios (7.79 − 132, mean = 37.8) than Grt I and

Table 2

LA-ICP-MS analysis results (in ppm) of garnet from Hongshan Cu polymetallic deposit.

Garnet type	Grt I										
Sample number	HS11-2-C1-03	HS11-2-C1-04	HS11-2-C2-01	HS11-2-C2-02	HS11-2-C3-01	HS11-2-C3-02	HS11-2-C4-01	HS11-2-C4-03	HS11-2-C5-01	HS11-2-C5-02	HS11-2-C5-03
Description	dark gray	dark gray	dark gray	dark gray	dark gray	dark gray	dark gray	dark gray	dark gray	dark gray	dark gray
Na	13.6	11.3	9.52	17.6	19.3	12.9	18.0	b.d.l.	17.0	12.0	b.d.l.
Mg	1651	1672	1316	1512	1243	1700	1234	1650	1339	1457	1632
Al	58,934	55,531	61,732	61,350	52,110	53,166	50,196	54,791	56,660	56,883	58,142
Si	178,192	154,810	147,847	173,227	165,820	156,522	166,653	146,934	152,107	154,493	175,765
K	b.d.l.	b.d.l.	b.d.l.	27.7	b.d.l.	b.d.l.	b.d.l.	b.d.l.	18.5	b.d.l.	b.d.l.
Ca	240,157	239,006	240,872	244,925	240,807	240,807	239,006	239,342	242,494	241,508	245,396
Sc	65.9	53.8	35.3	55.1	105	75.6	21.2	66.2	52.5	49.6	28.2
Ti	12,632	12,243	11,063	11,877	12,236	12,958	10,203	12,676	11,838	12,166	9049
V	113	51.2	36.1	43.2	177	58.7	138	55.5	42.8	120	713
Cr	107	58.4	21.6	41.1	75.0	130	24.4	50.8	37.3	20.4	305
Mn	5763	5067	5555	6031	5491	4847	4809	4905	4946	4829	5071
Fe	121,330	109,866	101,061	118,433	130,298	116,701	134,781	108,013	110,067	109,827	125,481
Sr	b.d.l.	0.06	b.d.l.	0.07	b.d.l.	b.d.l.	b.d.l.	b.d.l.	0.11	b.d.l.	b.d.l.
Y	137	59.4	132	115	399	77.0	175	70.8	100	107	63.2
Zr	403	316	315	338	450	337	421	286	399	389	153
Hf	18.8	16.2	15.2	16.3	25.3	17.1	14.4	14.7	18.9	14.8	6.7
W	24.0	11.2	37.0	37.3	45.4	8.76	116	6.01	47.9	40.0	2.45
Pb	0.07	0.26	b.d.l.	0.68	0.33	0.07	0.22	0.10	0.79	0.02	0.23
Th	0.08	0.29	b.d.l.	0.04	0.06	0.69	0.09	0.63	0.19	0.01	0.92
U	20.5	16.3	19.4	22.5	21.5	20.6	37.9	17.2	25.3	22.6	15.5
La	0.13	0.27	0.11	0.12	0.32	0.10	0.87	0.06	0.20	0.13	0.08
Ce	1.56	2.01	1.14	1.85	2.43	1.61	6.73	0.97	2.06	1.42	1.67
Pr	0.72	0.83	0.59	1.00	0.87	0.83	0.83	2.06	0.54	0.85	0.55	0.90
Nd	6.42	9.55	6.76	11.3	9.30	9.72	15.3	7.23	8.63	5.10	13.4
Sm	4.66	6.39	5.91	9.35	9.70	7.64	8.90	6.42	6.51	4.23	12.3
Eu	3.46	2.72	6.60	5.81	4.82	3.12	3.90	2.75	6.22	3.35	4.69
Gd	12.1	8.25	12.3	14.9	26.5	10.8	16.5	8.67	9.85	9.91	15.9
Tb	2.55	1.36	2.43	2.57	6.36	1.79	3.13	1.47	1.78	2.02	2.08
Dy	20.6	9.55	18.6	17.6	57.6	12.3	26.4	10.8	13.7	16.2	12.0
Ho	4.85	2.18	4.30	3.94	14.2	2.82	6.09	2.50	3.37	3.90	2.31
Er	16.8	7.47	15.3	13.7	49.6	9.41	21.6	8.57	12.2	13.2	6.63
Tm	2.39	1.03	2.41	1.96	7.29	1.32	3.28	1.34	1.87	2.08	0.84
Yb	18.0	7.79	16.8	12.8	49.6	9.60	25.0	9.86	13.2	15.0	5.99
Lu	3.10	1.23	2.31	1.75	7.00	1.40	3.44	1.38	1.94	2.27	0.77
Ti + Zr + Hf	13,053	12,575	11,394	12,232	12,711	13,312	10,638	12,977	12,255	12,570	9209
ΣREE	97.3	60.6	95.6	98.7	246	72.5	143	62.5	82.4	79.4	79.5
LREE	16.9	21.8	21.1	29.4	27.5	23.0	37.8	18.0	24.5	14.8	33.0
HREE	80.4	38.9	74.5	69.3	218	49.5	106	44.5	57.9	64.6	46.5
LREE/HREE	0.21	0.56	0.28	0.43	0.13	0.47	0.36	0.40	0.42	0.23	0.71
La_N/Yb_N	0.00	0.03	0.00	0.01	0.00	0.01	0.02	0.00	0.01	0.01	0.01
δEu	1.33	1.15	2.31	1.50	0.86	1.05	0.97	1.12	2.37	1.52	1.03
δCe	0.63	0.67	0.56	0.55	0.76	0.57	0.87	0.53	0.69	0.73	0.56

Garnet type	Grt II										
Sample number	HS11-1-C1-03	HS11-1-C1-06	HS11-1-C1-07	HS11-1-C1-08	HS11-1-C1-10	HS11-1-C1-11	HS11-1-C1-16	HS11-1-C1-17	HS11-1-C1-18	HS11-1-C2-14	HS11-1-C2-15
Description	dark gray	slightly bright gray	dark gray	bright gray	bright gray	bright gray	dark gray	bright gray	dark gray	bright gray	bright gray
Na	b.d.l.	b.d.l.	5.99	b.d.l.	b.d.l.	6.82	b.d.l.	b.d.l.	b.d.l.	b.d.l.	b.d.l.
Mg	852	879	1240	1520	1500	748	790	669	692	1191	841
Al	54,583	506	56,052	1879	1490	345	53,963	1864	53,286	333	565
Si	163,590	153,816	142,415	145,899	145,155	131,528	153,916	162,468	163,579	137,962	154,530
K	b.d.l.	b.d.l.	b.d.l.	b.d.l.	b.d.l.	b.d.l.	b.d.l.	15.3	b.d.l.	b.d.l.	b.d.l.
Ca	242,265	240,729	244,717	237,408	237,839	232,201	240,931	234,257	244,047	235,882	235,882
Sc	7.87	0.63	28.1	0.20	0.33	0.53	3.86	0.48	2.68	0.34	0.54
Ti	2627	11.3	5015	15.0	20.3	7.65	1632	7.72	732	19.1	13.3
V	47.7	7.66	64.6	7.37	6.61	5.63	47.0	10.5	28.4	3.80	5.29
Cr	b.d.l.	b.d.l.	115	b.d.l.	1.19	b.d.l.	b.d.l.	b.d.l.	b.d.l.	b.d.l.	b.d.l.
Mn	4848	1660	4291	1101	1087	1671	4659	1703	5078	961	1754
Fe	137,864	215,096	116,515	205,256	207,155	200,996	130,407	213,695	141,324	199,928	214,818
Sr	b.d.l.	b.d.l.	0.14	0.04	0.03	0.03	b.d.l.	0.07	b.d.l.	0.03	b.d.l.
Y	76.2	1.45	119	8.18	6.30	0.87	68.9	0.81	31.3	1.51	1.46
Zr	111	0.50	209	0.18	0.33	0.22	70.6	0.37	38.3	0.47	0.62
Hf	3.08	b.d.l.	7.59	b.d.l.	0.03	b.d.l.	1.61	b.d.l.	0.83	b.d.l.	b.d.l.
W	56.3	9.76	48.3	0.65	0.80	5.61	61.2	5.92	42.9	0.88	9.49
Pb	b.d.l.	b.d.l.	0.08	0.03	b.d.l.	0.16	0.04	0.18	0.13	0.03	0.08
Th	3.28	0.19	6.35	0.14	0.30	0.18	3.47	0.23	4.57	0.46	0.21
U	15.0	5.07	19.5	3.82	3.67	4.60	15.1	1.77	12.0	2.22	5.70
La	0.34	6.11	0.36	7.72	6.37	6.25	0.35	2.13	0.33	4.29	6.51
Ce	4.16	10.8	4.42	15.8	11.5	10.4	4.73	4.87	5.08	5.75	11.4

Table 2 (*continued*)

Pr	1.98	1.04	1.99	2.38	1.63	1.02	2.09	0.65	2.29	0.62	1.16
Nd	22.8	2.96	22.4	9.61	6.57	3.28	24.9	2.80	26.9	2.41	3.79
Sm	14.5	0.42	12.3	1.25	1.22	0.19	15.7	0.40	15.7	0.37	0.25
Eu	6.61	0.26	7.37	0.71	0.56	0.30	7.02	0.18	9.52	0.17	0.39
Gd	16.5	0.36	12.7	1.43	1.09	0.24	17.5	0.29	13.1	0.19	0.34
Tb	2.20	0.05	1.89	0.16	0.14	0.04	2.21	0.02	1.46	0.04	0.04
Dy	12.4	0.23	14.0	1.21	0.82	0.16	12.4	0.21	7.08	0.27	0.33
Ho	2.48	0.04	3.51	0.22	0.15	0.04	2.26	b.d.l.	1.08	0.05	0.04
Er	7.87	0.09	11.0	0.58	0.49	0.05	6.33	0.11	2.55	0.12	0.11
Tm	1.13	b.d.l.	1.57	0.06	0.04	b.d.l.	0.93	b.d.l.	0.28	0.01	b.d.l.
Yb	7.90	0.07	10.1	0.33	0.25	b.d.l.	6.34	0.10	1.81	0.07	b.d.l.
Lu	0.97	b.d.l.	1.49	0.03	0.04	b.d.l.	0.75	b.d.l.	0.27	0.01	b.d.l.
Ti + Zr + Hf	2741	11.8	5231	15.2	20.7	7.87	1704	8.09	771	19.6	13.9
ΣREE	102	22.4	105	41.5	30.9	22.0	103	11.8	87.4	14.4	24.4
LREE	50.3	21.5	48.8	37.5	27.8	21.5	54.8	11.0	59.7	13.6	23.5
HREE	51.5	0.82	56.2	4.03	3.03	0.54	48.7	0.74	27.6	0.76	0.86
LREE/HREE	0.98	26.2	0.87	9.30	9.18	40.1	1.12	14.9	2.16	18.0	27.3
La$_N$/Yb$_N$	0.03	64.4	0.03	16.8	18.0	8.01	0.04	14.7	0.13	44.6	7.12
δEu	1.30	2.04	1.79	1.62	1.46	4.29	1.29	1.57	1.98	1.69	4.14
δCe	0.61	0.96	0.64	0.90	0.85	0.92	0.66	1.00	0.65	0.76	0.94

Garnet type	Grt II										
Sample number	HS11-1-C2-16	HS11-1-C2-17	HS11-1-C2-18	HS11-1-C2-19	HS11-1-C2-21	HS11-1-C3-01	HS11-1-C3-02	HS11-1-C3-03	HS11-1-C3-04	HS11-1-C3-05	HS11-1-C3-06
Description	bright gray	dark gray	dark gray	dark gray	dark gray	dark gray	bright gray	dark gray	bright gray	dark gray	bright gray
Na	b.d.l.	b.d.l.	b.d.l.	b.d.l.	b.d.l.	b.d.l.	b.d.l.	b.d.l.	b.d.l.	b.d.l.	b.d.l.
Mg	836	999	947	1046	871	748	1026	866	997	1182	1216
Al	699	56,453	53,481	59,159	57,097	56,045	2574	54,195	319	47,366	1257
Si	134,169	181,201	161,544	183,291	154,165	154,026	149,873	159,861	158,875	158,860	161,441
K	b.d.l.	b.d.l.	b.d.l.	b.d.l.	b.d.l.	b.d.l.	7.48	b.d.l.	b.d.l.	b.d.l.	b.d.l.
Ca	235,361	244,987	236,063	244,616	242,359	243,702	236,090	242,609	235,868	241,065	236,411
Sc	0.49	4.78	4.86	3.62	3.76	2.75	0.43	4.55	0.92	48.1	0.53
Ti	11.4	3496	3065	2835	2011	949	14.1	1466	11.5	4428	39.4
V	4.67	48.2	47.2	56.2	38.6	34.0	9.40	46.9	11.1	61.9	6.27
Cr	b.d.l.	b.d.l.	3.06	3.61	b.d.l.	b.d.l.	b.d.l.	b.d.l.	b.d.l.	178	b.d.l.
Mn	1452	5019	4755	5394	4841	5208	2127	5007	1684	4090	1094
Fe	198,240	145,245	128,014	145,062	123,743	129,395	207,825	134,973	218,851	136,441	207,783
Sr	0.03	0.08	b.d.l.	b.d.l.	b.d.l.	b.d.l.	0.10	0.04	b.d.l.	0.03	0.06
Y	1.50	69.0	64.5	136	69.0	27.6	0.90	73.8	0.71	84.4	7.49
Zr	0.43	128	112	117	84.3	46.9	b.d.l.	68.7	0.40	197	0.99
Hf	b.d.l.	3.33	3.08	2.79	1.86	0.97	b.d.l.	1.94	b.d.l.	7.77	b.d.l.
W	21.2	70.9	61.7	61.2	55.1	34.4	18.8	74.1	8.04	91.8	0.99
Pb	b.d.l.	0.19	0.08	b.d.l.	0.07	0.05	0.34	0.06	0.15	0.16	0.04
Th	0.23	4.33	4.23	2.59	3.53	4.13	0.16	3.56	0.10	17.7	2.48
U	10.9	19.6	18.5	16.2	15.8	9.26	4.01	18.5	4.09	28.6	4.38
La	6.21	0.52	0.44	0.26	0.33	0.21	5.19	0.49	6.02	0.99	5.26
Ce	14.6	5.18	5.05	3.93	4.36	3.20	7.03	5.83	8.47	10.6	10.7
Pr	1.74	2.37	2.16	1.72	2.09	1.62	0.82	2.50	0.81	4.29	1.75
Nd	6.78	24.4	21.8	17.9	21.0	18.0	2.62	27.6	2.11	39.1	8.19
Sm	0.77	10.6	9.67	8.43	10.74	9.37	0.39	18.1	0.43	16.5	1.72
Eu	0.65	6.34	5.76	5.05	6.08	6.99	0.18	7.78	0.23	8.00	0.56
Gd	0.63	11.2	10.1	11.8	11.9	8.49	0.27	19.4	b.d.l.	13.4	1.08
Tb	0.03	1.56	1.45	2.30	1.65	0.96	0.04	2.38	0.04	1.77	0.15
Dy	0.30	10.9	9.62	18.1	11.4	5.38	0.15	13.2	b.d.l.	11.9	1.04
Ho	0.06	2.22	2.03	4.38	2.14	0.94	0.03	2.42	b.d.l.	2.58	0.21
Er	0.11	7.18	6.45	14.3	6.96	2.53	0.10	7.19	b.d.l.	8.12	0.67
Tm	b.d.l.	0.87	0.79	2.02	0.93	0.28	0.01	1.05	b.d.l.	1.10	0.07
Yb	0.06	6.23	5.74	14.1	5.89	2.15	0.05	6.92	0.10	7.95	0.35
Lu	b.d.l.	0.89	0.85	1.85	0.81	0.28	b.d.l.	0.86	b.d.l.	1.14	0.05
Ti + Zr + Hf	11.8	3628	3180	2955	2098	997	14.1	1537	11.9	4633	40.4
ΣREE	32.0	90.4	82.0	106	86.4	60.4	16.9	116	18.2	127	31.8
LREE	30.8	49.4	44.9	37.29	44.6	39.4	16.2	62.3	18.1	79.5	28.2
HREE	1.18	41.0	37.1	68.8	41.8	21.0	0.64	53.4	0.14	48.0	3.62
LREE/HREE	26.0	1.21	1.21	0.54	1.07	1.88	25.2	1.17	132	1.66	7.79
La$_N$/Yb$_N$	78.8	0.06	0.06	0.01	0.04	0.07	68.9	0.05	42.5	0.09	10.7
δEu	2.78	1.77	1.76	1.55	1.63	2.35	1.65	1.26	1.68	1.60	1.16
δCe	1.07	0.62	0.67	0.67	0.61	0.59	0.75	0.67	0.82	0.70	0.86

Garnet type	Grt II							
Sample number	HS11-1-C3-07	HS11-1-C6-01	HS11-1-C6-02	HS11-1-C6-03	HS11-1-C6-04	HS11-1-C6-05	HS11-1-C6-06	HS11-1-C6-07
Description	dark gray	slightly bright gray	dark gray	bright gray	dark gray	bright gray	dark gray	dark gray
Na	b.d.l.	11.5	b.d.l.	b.d.l.	b.d.l.	b.d.l.	b.d.l.	b.d.l.
Mg	1568	768	1064	938	983	1442	783	1618
Al	62,096	31,738	58,131	93.8	48,808	639	50,165	62,122
Si	171,900	149,811	158,782	151,991	155,415	155,436	156,415	155,312
K	b.d.l.	7.48	b.d.l.	b.d.l.	4.82	b.d.l.	b.d.l.	b.d.l.
Ca	253,523	241,651	244,531	234,839	241,601	235,775	249,156	243,895

Table 2 (continued)

Sc	11.6	b.d.l.	3.33	0.66	18.7	b.d.l.	1.14	14.6
Ti	6847	25.9	3202	1.97	2741	23.6	2446	6764
V	245	49.1	50.0	0.46	50.0	3.56	180	201.1
Cr	45.1	b.d.l.	b.d.l.	b.d.l.	b.d.l.	58.36	b.d.l.	30.9
Mn	4244	3143	4902	1579	4200	1009	1926	4200
Fe	120,462	158,805	123,105	210,320	131,763	201,413	127,544	105,276
Sr	b.d.l.	0.09	b.d.l.	b.d.l.	0.21	b.d.l.	b.d.l.	b.d.l.
Y	251	42.0	78.8	0.17	81.6	1.61	384	177
Zr	217	0.98	110	0.16	129	0.37	61.9	188
Hf	6.31	0.03	2.33	b.d.l.	3.88	b.d.l.	0.71	6.38
W	23.8	525	72.5	6.43	114	3.05	1.30	17.7
Pb	0.10	0.38	0.11	b.d.l.	0.16	0.08	0.04	0.05
Th	3.32	7.91	3.62	0.07	10.9	1.09	2.83	2.11
U	11.4	95.6	22.5	2.90	27.7	8.18	4.19	10.4
La	0.44	6.08	0.53	4.15	1.30	7.96	0.34	0.34
Ce	6.03	42.2	6.07	5.97	12.8	17.6	3.87	5.34
Pr	2.68	11.7	2.66	0.38	4.89	2.45	1.89	2.54
Nd	28.1	77.2	24.6	0.90	44.6	8.96	22.6	26.0
Sm	14.5	20.4	11.5	b.d.l.	19.8	1.15	11.6	13.1
Eu	3.69	9.91	6.24	0.15	10.2	0.46	1.99	3.39
Gd	20.0	15.9	11.9	0.14	14.6	0.39	19.5	16.2
Tb	3.85	1.85	1.94	b.d.l.	1.95	0.07	4.08	2.89
Dy	29.4	9.01	12.9	b.d.l.	11.5	0.34	35.5	21.5
Ho	6.75	1.35	2.51	b.d.l.	2.45	0.03	9.20	4.96
Er	22.8	2.88	7.80	0.05	7.27	0.13	33.0	15.5
Tm	3.19	0.22	0.98	b.d.l.	0.97	0.02	4.36	2.26
Yb	22.8	1.15	6.35	b.d.l.	6.56	0.23	29.8	15.3
Lu	4.15	0.10	0.94	b.d.l.	0.88	0.02	3.98	2.34
Ti + Zr + Hf	7071	26.9	3314	2.12	2874	24.0	2508	6958
ΣREE	168	200	96.8	11.7	140	39.8	182	132
LREE	55.4	167	51.5	11.5	93.6	38.6	42.3	50.6
HREE	113	32.4	45.3	0.19	46.3	1.23	139	81.0
LREE/HREE	0.49	5.16	1.14	60.0	2.02	31.4	0.30	0.63
La_N/Yb_N	0.01	3.80	0.06	7.12	0.14	25.1	0.01	0.02
δEu	0.66	1.62	1.62	7.78	1.75	1.69	0.40	0.71
δCe	0.66	0.93	0.66	0.91	0.73	0.97	0.59	0.62

Note: b.d.l. = below detection limit.

Grt II Al-rich zones. In the primitive mantle-normalized diagram (Fig. 9), the Grt II Fe-rich zones are strongly enriched in LREE and depleted in HREE with pronounced positive Eu anomalies.

6. Discussion

6.1. Mechanism of REE substitution into garnet

Trace elements in garnets, especially REEs, can be used to trace fluid source and fluid-rock interactions (Giuliani et al., 1987; Vander Auwera and Andre, 1991). This is because REEs (La-Lu) have very similar chemical properties due to their similar ionic radius and ionic charge, and are able to fractionate from one another under specific geological environment (Smith et al., 2004). The general formula of garnet can be expressed as $X_3Y_2Z_3O_{12}$, where X site is occupied by divalent cations (e.g., Ca^{2+}, Mg^{2+}, Mn^{2+} or Fe^{2+}) in eight-fold coordination, Y site is trivalent cations (e.g., Al^{3+}, Cr^{3+} or Fe^{3+}) in an octahedral coordination, and Z site is mainly Si in tetrahedral coordination (Menzer, 1926; Gaspar et al., 2008). It is well accepted that REEs substitution into garnet occurs in the dodecahedral site by replacing divalent cations, such as Ca^{2+} (Carlson, 2012). The presence of magnetite and pyrrhotite at Hongshan indicates a relatively reduced environment (fO_2 below hematite-magnetite buffer), in which Eu^{2+} ions would be predominant in the hydrothermal fluid (Gaspar et al., 2008). This favors the substitution of Ca^{2+} by Eu^{2+} in the X site. However, since the substitution of REE^{3+} into garnet is heterovalent, coupled substitutions are required to maintain the charge balance (Gaspar et al., 2008; Carlson, 2012; Park et al., 2017b). Previous studies suggested that the charge balance can be achieved by the following substitutions (Jaffe, 1951; Enami et al., 1995; Quartieri et al., 1999a, 1999b; Grew et al., 2010; Carlson, 2012):

$$[X^{2+}]_{-2}^{VIII} [X^+]_{+1}^{VIII} [REE^{3+}]_{+1}^{VIII} \tag{1}$$

$$[X^{2+}]_{-1}^{VIII} [REE^{3+}]_{+1}^{VIII} [Si^{4+}]_{-1}^{IV} [Z^{3+}]_{+1}^{IV} \tag{2}$$

$$[X^{2+}]_{-1}^{VIII} [REE^{3+}]_{+1}^{VIII} [Y^{3+}]_{-1}^{VI} [Y^{2+}]_{+1}^{VI} \tag{3}$$

$$[X^{2+}]_{-3}^{VIII} []_{+1}^{VIII} [REE^{3+}]_{+2}^{VIII} \tag{4}$$

(X^+ represents Na^+; X^{2+} is mainly by Ca^{2+}; Z^{3+} represents Al^{3+} or Fe^{3+}; Y^{3+} substituted mainly by Al^{3+}; Y^{2+} represents Mg^{2+} or Fe^{2+}; [ ] is a Ca site vacancy, VIII, VI and IV represent 8, 6 and 4 coordination, respectively).

The REE^{3+} incorporation into garnet via Eq. (1) could form Na-bearing garnet (Enami et al., 1995). However, the Na_2O contents of garnets in this study are far below those of the Na-bearing garnets (up to 0.37 wt% Na_2O), from Su-Lu terrane in Eastern China (Enami et al., 1995), indicating that the Na_2O contents of garnet at Hongshan are too low to balance the charge (Table 1) (Peng et al., 2015; Park et al., 2017b). Moreover, the Na contents do not display liner relationship with the REE^{3+} contents (Table 2), which further implies that the REE^{3+} incorporated into garnet did not follow the Eq. (1) substitution mechanism. The Eq. (2) mechanism involves charge compensation by substituting trivalent cations into the tetrahedral site (Jaffe, 1951; Gaspar et al., 2008; Xu et al., 2016). However, neither the total Al or Fe^{3+} contents correlate with the REE^{3+} contents (Fig. 10a and b), suggesting that the "yttrogarnet" (YAG)-type substitution is not the main substitution mechanism (Gaspar et al., 2008; Park et al., 2017b; Xiao et al., 2018). The positive ΣREE^{3+} vs. Mg (Fig. 10c), and negative ΣREE^{3+} vs. Fe^{2+} correlations (Fig. 10d) suggest that REE^{3+} incorporated into Grt II probably followed Eq. (3) (i.e., the menzerite substitution) (Grew et al., 2010; Carlson, 2012). Nevertheless, Grt I does not show clear Mg vs. ΣREE^{3+} or Fe^{2+} vs. ΣREE^{3+} correlations, implying that Eq (3) was not the key substitution mechanism for Grt I, either. Therefore, the REE^{3+} incorporation into Grt I possibly followed the Eq. (4) mechanism via Ca site vacancy (Quartieri et al., 1999a,b).
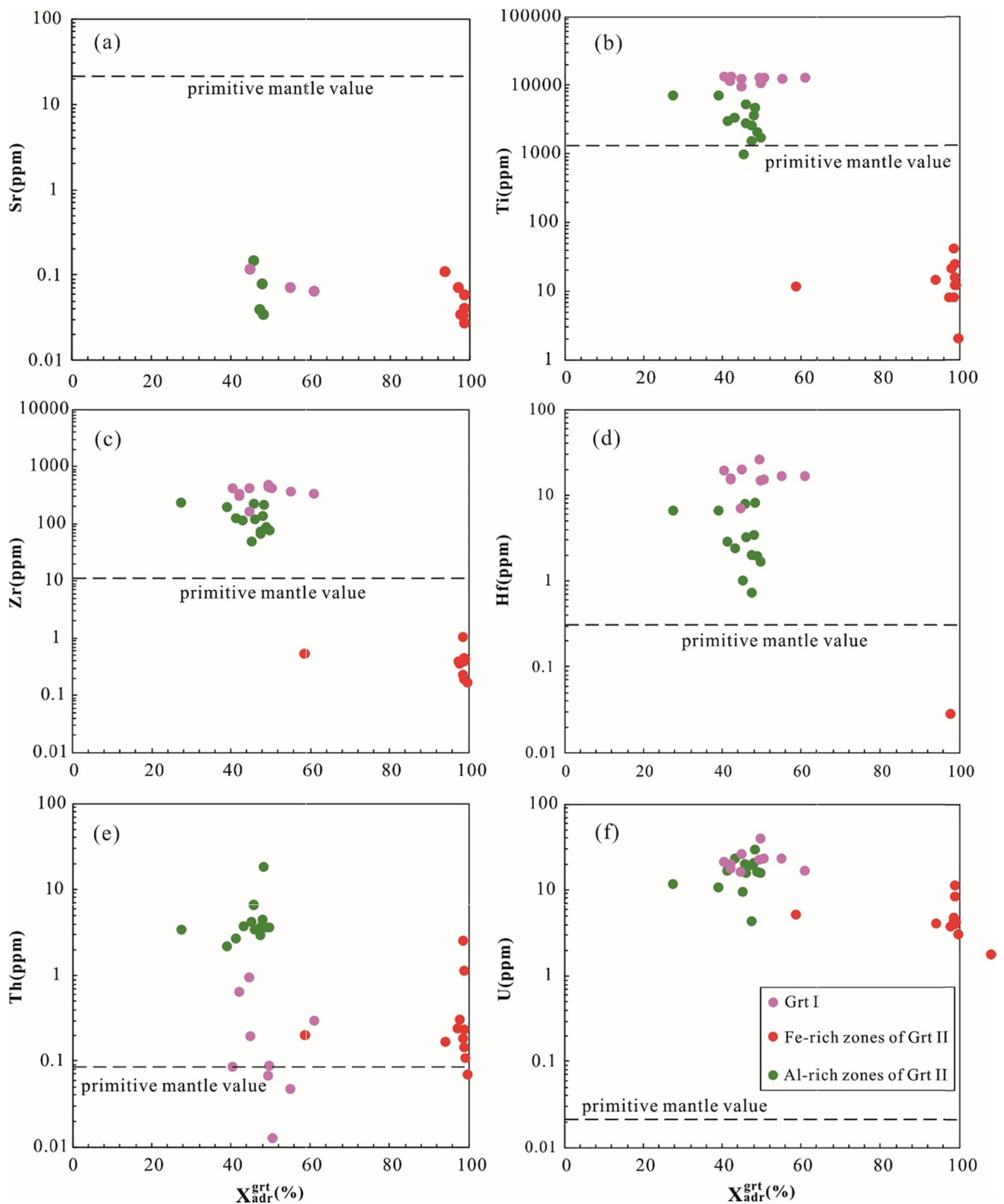
Fig. 8. Binary plots for the trace elements in the garnet at Hongshan. Primitive mantle values are from Sun and McDonough (1989).

Yttrium (Y) has very similar geochemical behavior to REE^{3+}. Assuming the REE^{3+} and Y incorporation into garnet was solely controlled by crystal chemistry (e.g., coupled substitution mechanism), strong correlations between REE^{3+} vs. Y and Ca should be observed (Dziggel et al., 2009; Park et al., 2017b). However, such correlations are not observed in our studied samples (Fig. 10e-f). For Grt II, the Al-rich zones have higher Ca and ΣREE contents than the Fe-rich zones (Fig. 10f), which was probably caused by fluid chemical changes as previously reported in Navachab Au deposit, Namibia (Dziggel et al., 2009). Thus, apart from the coupled substitution mechanism, external
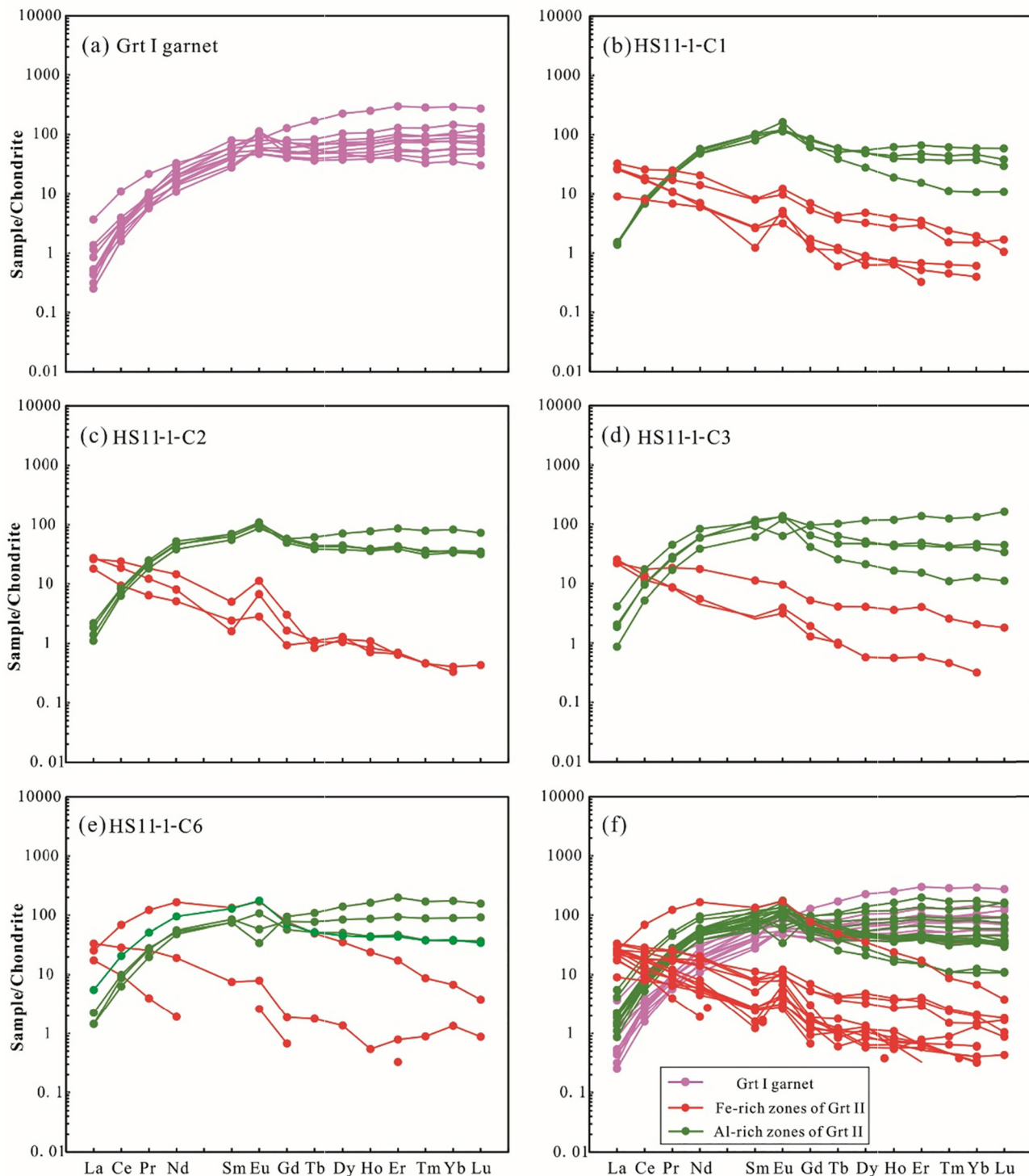
Fig. 9. Chondrite-normalized REE patterns of the garnet at Hongshan. Chondrite normalized values are from Sun and McDonough (1989).

factors such as fluid chemistry, physicochemical parameters (e.g., pH, fO_2) may also have influenced the REE incorporation into garnet crystal lattice (Gaspar et al., 2008; Dziggel et al., 2009; Zhai et al., 2014; Fu et al., 2018).

6.2. Physicochemical conditions of hydrothermal fluid

6.2.1. Oxygen fugacity (fO_2)

Redox-sensitive elements (e.g., U) can occur in different valence states (e.g., U^{4+} and U^{6+}) and their behaviors are significantly affected by fO_2 (Smith et al., 2004), making them an effective tool to estimate the redox state of hydrothermal fluids (Zhang et al., 2017a,b). Because the ionic radius of U^{4+} (1.000 Å) is more similar to the that of Ca^{2+} (1.120 Å) than U^{6+} (0.730 Å), it is expected that U^{4+} is more likely to substitute Ca^{2+} in garnet than U^{6+} (Smith et al., 2004; Gaspar et al., 2008; Zhang et al., 2017b). Therefore, U contents in Hongshan Grt I and Grt II can indicate the fO_2 of the skarn mineralization fluids.

As mentioned above, Grt I have higher U contents (15.5–37.9 ppm, mean 22.5 ppm) (Figs. 8f and 11; Table 2) than Grt II, indicating that it was formed under relatively low fO_2. Besides, U contents of Grt II alternate across the oscillatory growth zones (Fig. 12), with those of the
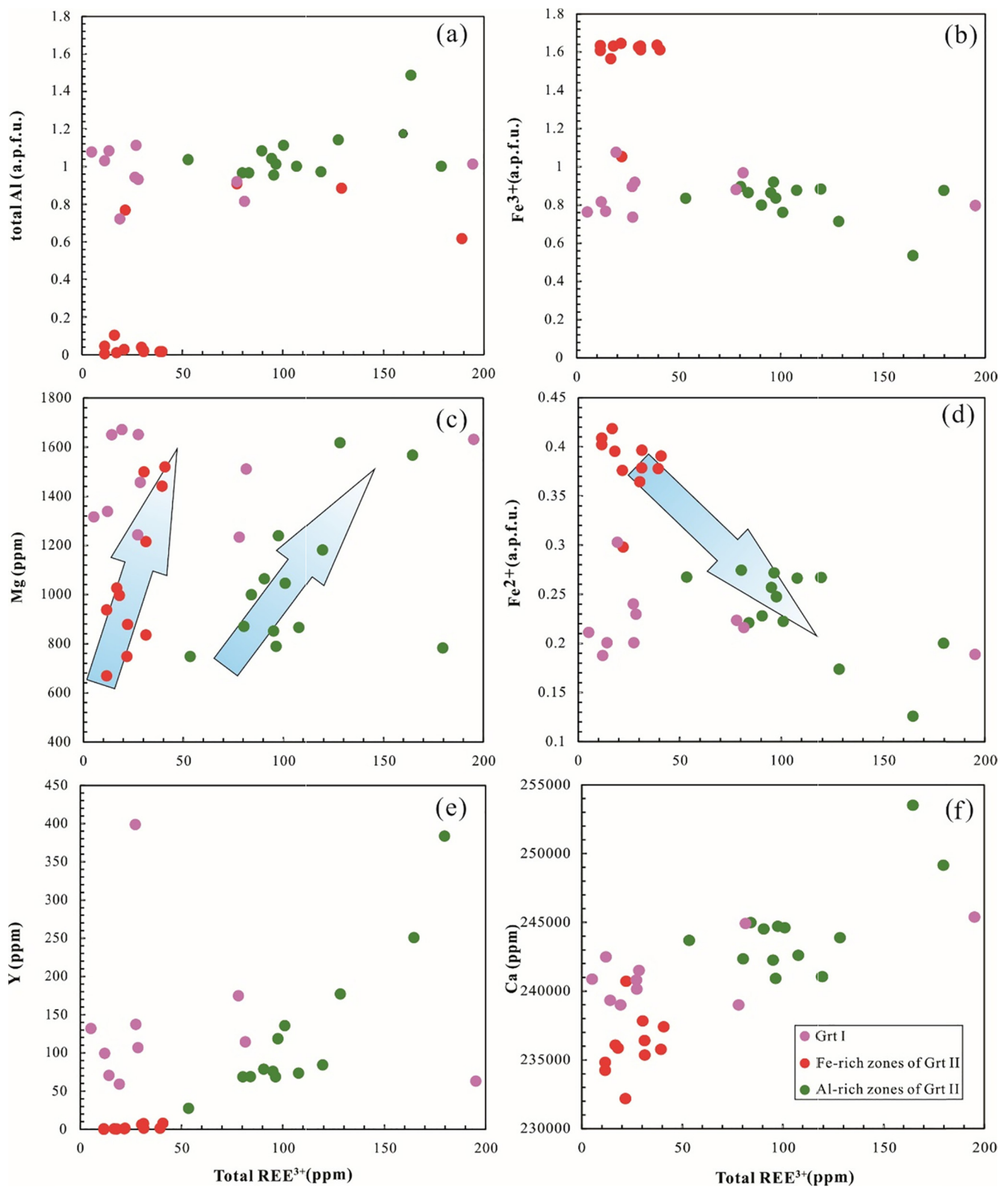
Fig. 10. Plots of total REE^{3+} with total Al, Fe^{3+}, Mg, Fe^{2+}, Y, and Ca of the garnet at Hongshan.

Al-rich zones being higher (4.19–28.6 ppm, mean 16.5 ppm) than the Fe-rich zones (1.77–10.9 ppm, mean 4.93 ppm). This implies that the Fe-rich zones were crystallized under higher fO_2. From the Grt II core to rim, the fluctuating U content likely reflect a dynamic redox fluctuation environment (Fig. 12).

6.2.2. pH

It is suggested that REE fractionation is dependent strongly on the hydrothermal fluid pH (Bau, 1991; Zhang et al., 2017b; Fu et al., 2018). Under mildly acidic conditions, the fluids are commonly LREE-enriched and HREE-depleted with positive Eu anomalies (Bau, 1991), whereas the nearly neutral fluids are HREE-enriched and LREE-depleted with
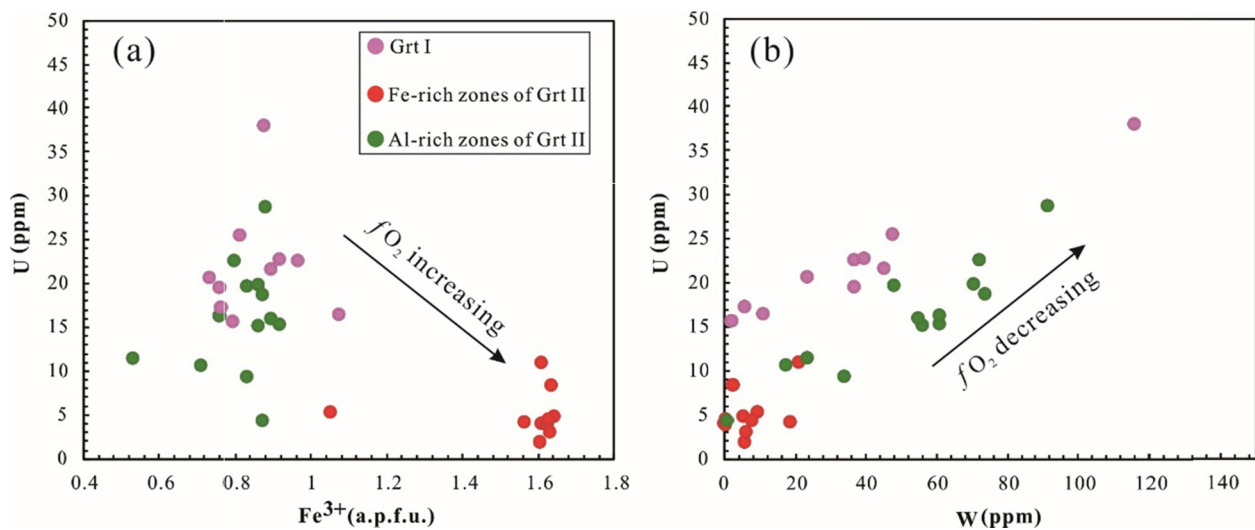
Fig. 11. (a) U versus Fe^{3+} and (b) U versus W diagrams for the garnet at Hongshan.

negative or no Eu anomalies (Zhang et al., 2017a, 2017b; Fu et al., 2018). Furthermore, the REE contents and chondrite-normalized patterns of the fluids are also controlled by the presence of Cl^-, which can transport Eu in$EuCl_4^{2-}$complex and form distinctly positive Eu anomalies (Allen and Seyfried, 2005; Zhai et al., 2014; Zhang et al., 2017b). At Hongshan, the presence of halite daughter mineral in fluid inclusions (Li et al., 2013; Peng et al., 2015) indicates that the hydrothermal fluids were Cl-rich. The Hongshan Grt I and Grt II Al-rich zones are strongly HREE-enriched and LREE-depleted with minor positive (and less commonly negative) Eu anomalies, suggesting that they were possibly crystallized from a nearly neutral and Cl-rich fluid (Park et al., 2017b; Zhang et al., 2017a; Xiao et al., 2018). In contrast, the Grt II Fe-rich zones are LREE-enriched and HREE-depleted with pronounced positive Eu anomalies, implying that they were crystallized from a mildly acidic fluid (Bau, 1991; Zhang et al., 2017a,b; Fu et al., 2018).

6.3. Formation of oscillatory zoning in garnet

Oscillatory zoning is common in hydrothermal garnets (Allegre et al., 1981; Yardley et al., 1991; Wang and Merino, 1992; Jamtveit et al., 1993; Shore and Fowler, 1996). Oscillatory zoning is suggested to be formed by: (1) Internal crystal growth processes, which involves spontaneous chemical self-organization controlled by kinetic factors, such as mineral growth rate and diffusion rate of key elements in the fluid, without any external influence (Allegre et al., 1981; Wang and Merino, 1992); (2) Cyclic variations of external factors (e.g., P-T, fO_2, and fluid chemistry) (Yardley et al., 1991; Jamtveit et al., 1993, 1995). Such zoning is likely formed mainly in altered rocks and can have very larger intra-grain compositional variations (Yardley et al., 1991; Jamtveit et al., 1995).

At Hongshan, compositions of the Grt II oscillatory zones vary widely (Figs. 8 and 9; Table 2). In general, the Al-rich zones contain much higher Al, Sc, Ti, V, Mn, Y, Zr, Hf, W, Th and U contents, but much lower Fe contents than the Fe-rich zones (Table 2). The Ti contents variation across different zones, for instance, is up to three orders of magnitude, and achieving that via chemical self-organization is highly unlikely (cf. Keankeo and Hermann, 2002; Kohn, 2004).

The coexistence of liquid-rich, vapor-rich, and multiphase fluid inclusions in the Grt II Fe-rich zones (Peng et al., 2015) suggests that Grt II may have formed via fluid boiling led by hydro-fracturing, as indicated by the presence of hydraulic breccias (Peng et al., 2014a; Wang et al., 2017a). Previous studies suggested that fluid boiling can significantly increase the fO_2 of the residual liquid (Yardley et al., 1991), and the activity of Fe^{3+} with respect to Al^{3+}, which favors andradite

precipitation (Jamtveit et al., 1993, 1995). This agrees with our suggestion that the Grt II Fe-rich zones were formed under higher fO_2 than the Al-rich zones. Moreover, the lower trace element contents in the Fe-rich zones are also consistent with the fluid dilution by meteoric water incursion due to hydro-fracturing.

In summary, we propose a conceptual model for the growth of Grt I and Grt II at Hongshan (Fig. 13). During early stage of skarn alteration, magmatic fluids exsolved from the quartz monzonite porphyry interacted with the calciferous wall rocks (i.e. limestone and sandy-slate of the Qugasi Formation), and formed Grt I via diffusive metasomatism under low W/R (water/rock) ratios (Peng et al., 2015). At late stage of skarn alteration, continuous accumulation of hydrothermal fluids (and thus pressure) may have resulted in hydro-fracturing (Peng et al., 2014a; Wang et al., 2017a). This subsequently triggered fluid boiling, as recorded by the fluid inclusions in Grt II (Peng et al., 2015). The boiling likely increased the fO_2 and Fe^{3+} activity (with respect to Al^{3+}) in the residual hydrothermal fluid and facilitated the formation of the Grt II Fe-rich zones. When the cracks were sealed by various hydrothermal veins, the original hydrothermal system was restored. In that case, the relatively low fO_2 but high Al^{3+} activity (with respect to Fe^{3+}) was favorable for the formation of Grt II Al-rich zones. Repeating crack-seal processes of the hydrothermal system ultimately formed the oscillatory-zoned garnets at Hongshan.

6.4. Fingerprinting skarn deposit types

Garnet, a common gangue mineral in most types of skarn deposits, hosts important genetic information of the hydrothermal fluid evolution and ore-forming environment. This makes garnet chemistry a potential powerful tool to discriminate various types of skarn mineralization.

The Sp (spessartine) + Al (almandine) – Gr (grossularite) – Ad (andradite) triangular plot proposed by Meinert (1992) shows the proportion of the four most abundant end-members of hydrothermal garnets. These major-element discrimination diagrams provide a baseline for the skarn deposits type classification, including W, Sn, Mo, Au, Zn, Cu and Fe skarns. Nonetheless, these diagrams have distinct limitation that different skarn deposit subtypes generally have significant overlaps. For example, the field of Fe skarn deposit and that of Au skarn deposit is nearly overlapped. Likewise, the Cu-skarn field overlaps largely with the Mo-skarn field.

Previous studies have shown that the concentrations of trace elements in garnet are a function of temperature, pressure, fO_2, pH, salinity, and composition of hydrothermal fluid (Jamtveit et al., 1995;
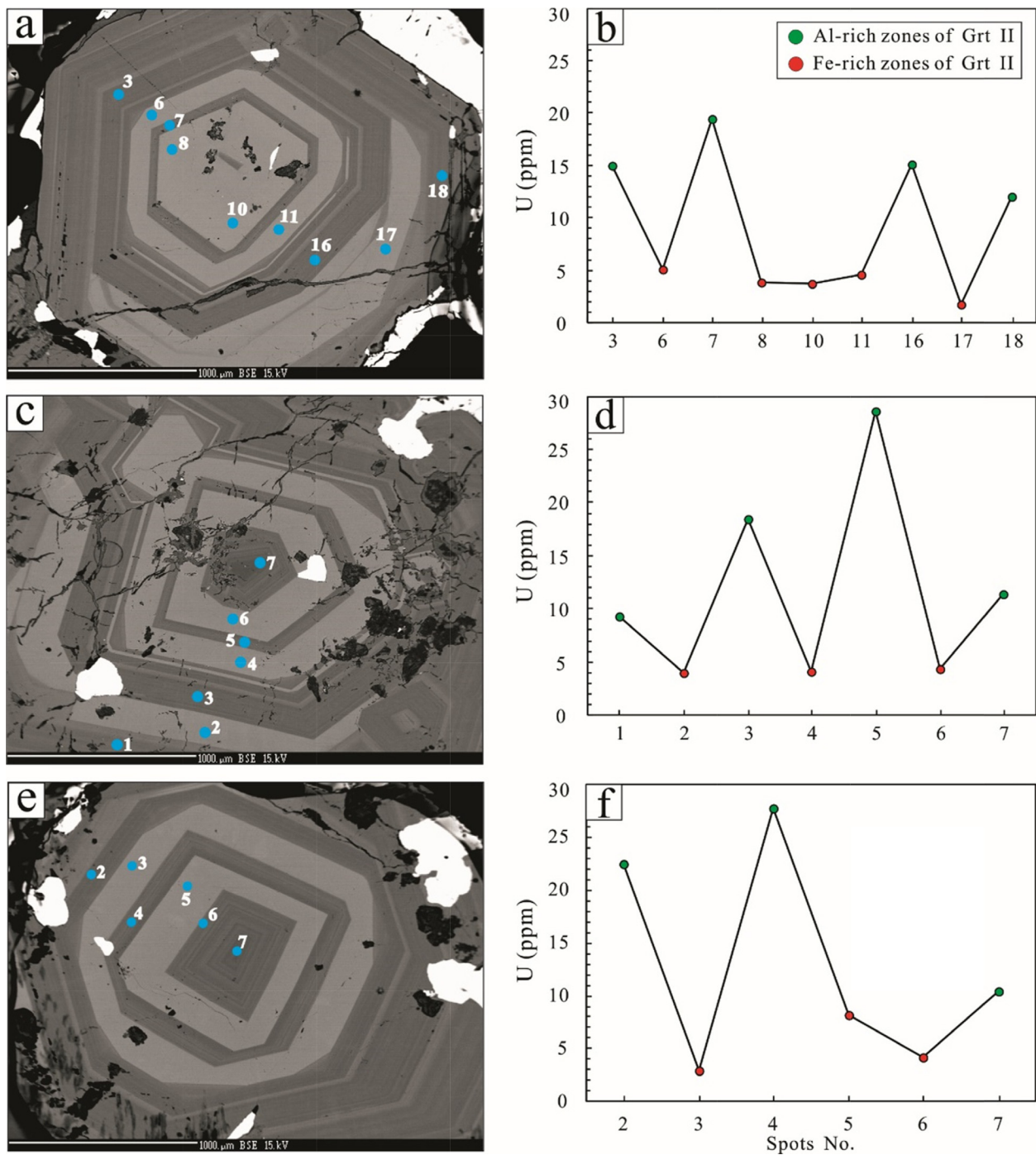
Fig. 12. BSE images and U concentrations profiles of the Garnet II at Hongshan. Blue dots and white numbers represent the LA-ICP-MS analysis spots and numbers, respectively. Green dots and red dots denote the analysis on the dark-gray (Al-rich) and bright-gray (Fe-rich) areas, respectively. (For interpretation of the references to color in this figure legend, the reader is referred to the web version of this article.)

Karimzadeh Somarin, 2004; Zhai et al., 2014; Park et al., 2017a; Zhang et al., 2017b; Zhou et al., 2017 and references therein). Thus, we can employ some elements (e.g., redox-sensitive elements, and/or P-T-dependent ones) to constrain the formation conditions of different types of skarn deposit. In this study, we attempt to use some widely-accepted redox-sensitive elements (e.g., U, Sn) to fingerprint different types of skarn deposit. We compile the garnet chemical data form various well-studied skarn deposits in Asia, including our data from Hongshan and published ones from the Sangdong-Weondong W skarn deposit (South Korea) (Park et al., 2017a,b), Huangshaping W skarn deposit (Hunan, South China) (Ding et al., 2018), Baiganhu W-Sn skarn deposit

(Xinjiang, NW China) (Zhou et al., 2017), Yongping Cu skarn deposit (Jiangxi, eastern China) (Zhang et al., 2017a), the Hongshan-Hongniu Cu skarn deposit (Yunnan, SW China) (Peng et al., 2015), Zhibula Cu deposit (Tibet, western China) (Xu et al., 2016), and the Xinqiao Cu-S-Fe-Au skarn deposit (Anhui, eastern China) (Zhang et al., 2017b; Xiao et al., 2018). The data were compared to establish a series of skarn discrimination diagrams, which are illustrated in Fig. 14.

In the plots of δEu vs. V and δCe vs. V, the W skarn field largely overlaps with the W-Sn and W-Mo skarn fields, yet the Cu skarn field is distinct from the W, W-Sn, and W-Mo skarn fields (Fig. 14a and b). In the δCe vs. U plot, the Cu skarn field largely overlaps with the W-Mo

18
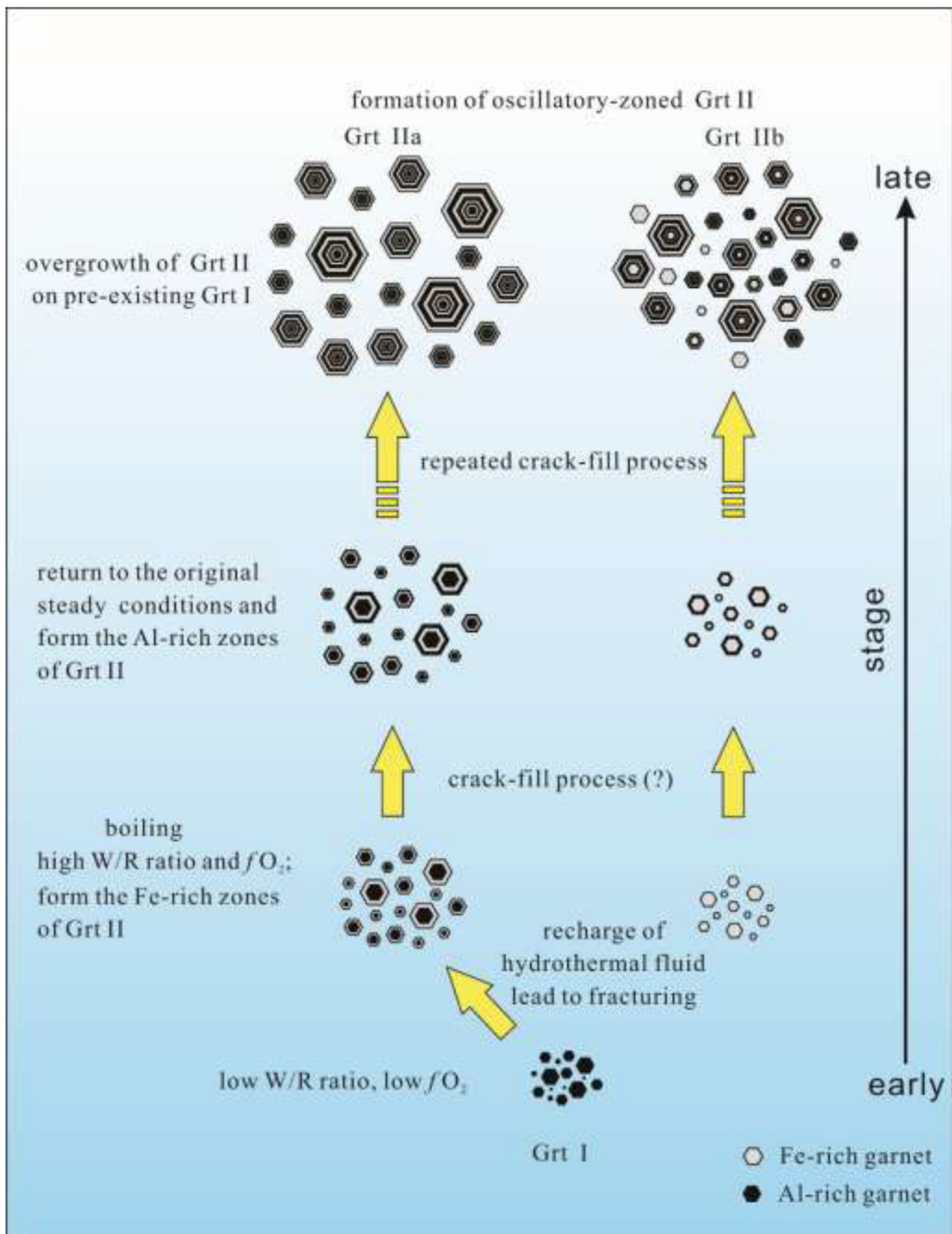
Fig. 13. A schematic diagram showing the formation process of oscillatory-zoned garnet at Hongshan. See text for details.

skarn field, overlaps partially with the W-Sn skarn field, but only overlaps slightly with the W skarn field (Fig. 14c). In the U vs. V plot, there is minor overlap between the Cu skarn, W and W-Mo skarn fields, yet the overlapping between the W and W-Sn skarn fields are severe (Fig. 14d). In the Sn vs. U plot, the Cu, W, and W-Mo skarn fields are

better separated, although there is still minor overlap between the W and W-Sn skarn fields (Fig. 14e). In the U vs. W plot, the four skarn fields are well separated (Fig. 14f).

Our study shows that garnets from the Cu, W, W-Mo, and W-Sn skarn deposits have different signatures and the above-mentioned
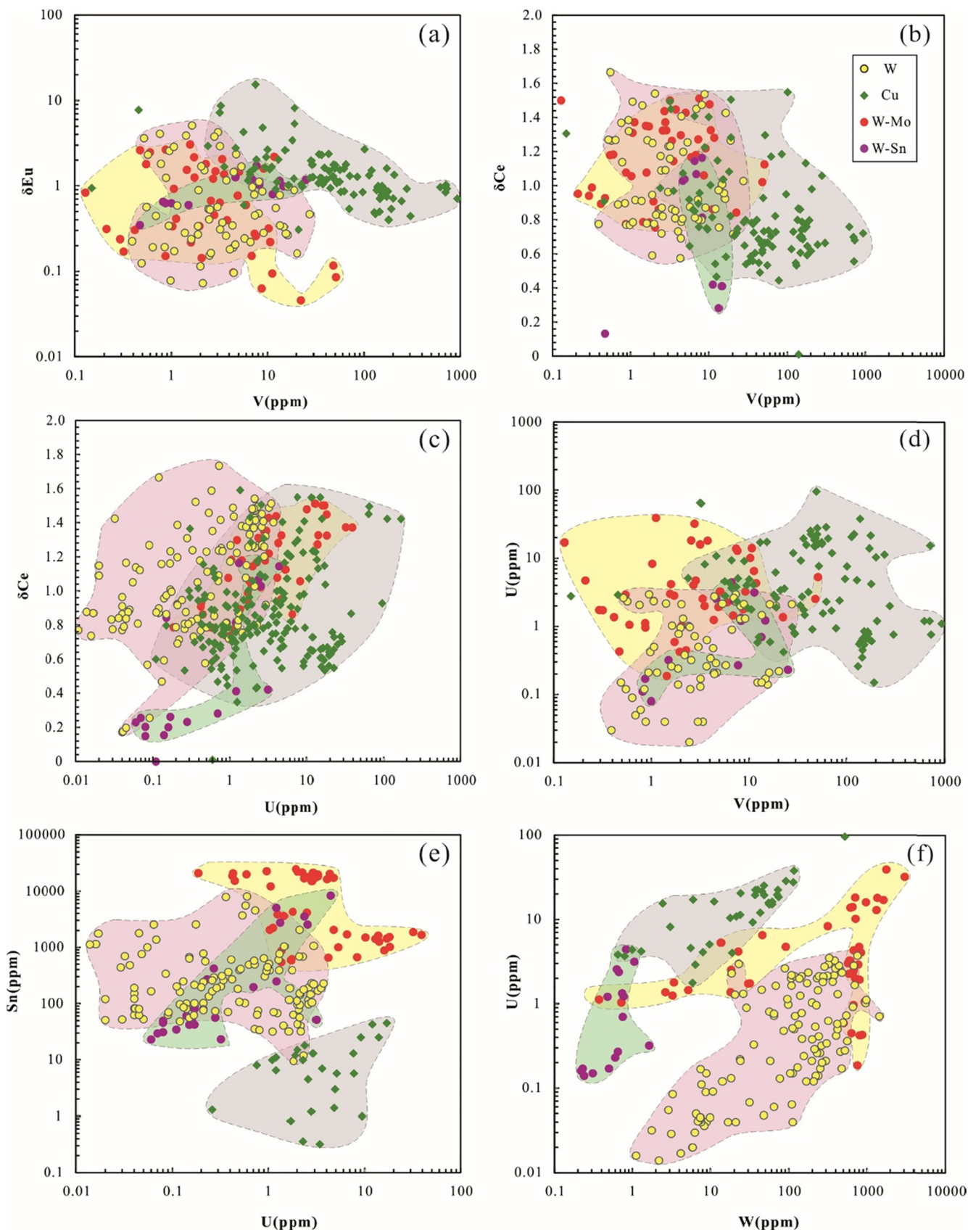
Fig. 14. Plots of δEu versus V (a), δCe versus V (b), δCe versus U (c), U versus V (d), Sn versus U (e), and U versus W (f) in garnets from different types of skarn deposits. Data are from this study, Peng et al. (2015), Xu et al. (2016), Park et al. (2017a,b), Zhang et al. (2017a,b), and Zhou et al. (2017), Ding et al. (2018), Xiao et al. (2018).

discrimination diagrams are effective to distinguish between typical Cu, W, W-Mo, and W-Sn skarn deposit. In addition, our dataset reveals that garnet in W-Sn skarn deposit contains high Sn content, whereas in W-Mo skarn deposit and Cu skarn deposit have high W and V contents, respectively.

7. Conclusions

(1) Garnets at Hongshan can be divided into the early-formed poorly-zoned Garnet I (Grt I) and the later-formed well-zoned Garnet II (Grt II). Grt I and the Grt II Al-rich zones belong mainly to grandite, while the Grt II Fe-rich zones range from grandite to almost pure andradite.

(2) Grt I and the Grt II Al-rich zones have similar REE patterns, with chondrite-normalized HREE enrichments, LREE depletions, and positive Eu anomalies. In contrast, the Grt II Fe-rich zones are strongly LREE-enriched and HREE-depleted with pronounced positive Eu anomalies.

(3) Incorporation of REEs into Grt I and Grt II was likely controlled by the substitution mechanism of $[X^{2+}]_{-3}^{VIII}[]_{+1}^{VIII}[REE^{3+}]_{+2}^{VIII}$ via a Ca site vacancy and the menzerite-type substitution, respectively. Physicochemical factors and the fluid compositions may also have played a role in the substitution.

(4) Grt I and the Grt II Al-rich zones were likely formed under a relatively reduced and near-neutral pH condition, whereas the Grt II Fe-rich zones were likely formed in a more oxidized and mildly acidic condition.

(5) Trace element discrimination diagrams of garnets are effective to distinguish different types of skarn deposits. Binary plots, such as δEu vs. V, δCe vs. U, and U vs. W, are useful to distinguish between typical Cu, W, W-Sn and W-Mo skarn deposits.

Acknowledgments

Appendix A. Supplementary data

Supplementary data to this article can be found online at https://doi.org/10.1016/j.oregeorev.2019.103016.

References

Allegre, C.J., Provost, A., Jaupart, C., 1981. Oscillatory zoning: a pathological case of crystal growth. Nature 294, 223–228.
Allen, D.E., Seyfried, W.E., 2005. REE controls in ultramafic hosted MOR hydrothermal systems: an experimental study at elevated temperature and pressure. Geochim. Cosmochim. Acta 69, 675–683.
Bau, M., 1991. Rare-earth element mobility during hydrothermal and metamorphic fluid rock interaction and the significance of the oxidation-state of europium. Chem. Geol. 93, 219–230.
Baxter, E.F., Caddick, M.J., Ague, J.J., 2013. Garnet: common mineral, uncommonly useful. Elements 9, 415–419.
Baxter, E.F., Scherer, E.E., 2013. Garnet geochronology: timekeeper of tectonometamorphic processes. Elements 9, 433–438.
Beyer, C., Frost, D.J., Miyajima, N., 2015. Experimental calibration of a garnet–clinopyroxene geobarometer for mantle eclogites. Contrib. Mineral. Petrol. 169, 18.
Blichert-Toft, J., Frei, R., 2001. Complex Sm-Nd and Lu-Hf isotope systematics in metamorphic garnets from the Isua supracrustal belt, West Greenland. Geochim. Cosmochim. Acta 65, 3177–3189.
Caddick, M.J., Kohn, M.J., 2013. Garnet: Witness to the evolution of destructive plate boundaries. Elements 9, 427–432.
Cao, K., Xu, J.F., Chen, J.L., Huang, X.X., Ren, J.B., Zhao, X.D., Liu, Z.X., 2016. Double-

layer structure of the crust beneath the Zhongdian arc, SW China: U-Pb geochronology and Hf isotope evidence. J. Asian Earth Sci. 115, 455–467.
Carlson, W.D., 2012. Rates and mechanism of Y, REE, and Cr diffusion in garnet. Am. Mineral. 97, 1598–1618.
Cheng, H., Vervoort, J.D., Dragovic, B., Wilford, D., Zhang, L.M., 2018. Coupled Lu-Hf and Sm-Nd geochronology on a single eclogitic garnet from the Huwan shear zone. China. Chem. Geol. 476, 208–222.
Crowe, D.E., Riciputi, L.R., Bezenek, S., Ignatiev, A., 2001. Oxygen isotope and trace element zoning in hydrothermal garnets: Windows into large-scale fluid-flow behavior. Geology 29, 479–482.
Ding, T., Ma, D.S., Lu, J.J., Zhang, R.Q., 2018. Garnet and scheelite as indicators of multi-stage tungsten mineralization in the Huangshaping deposit, southern Hunan province. China. Ore Geol. Rev. 94, 193–211.
Dziggel, A., Wulff, K., Kolb, J., Meyer, F.M., Lahaye, Y., 2009. Significance of oscillatory and bell-shaped growth zoning in hydrothermal garnet: evidence from the Navachab gold deposit. Namibia. Chem. Geol. 262, 266–276.
Enami, M., Cong, B., Yoshida, T., Kawabe, I., 1995. A mechanism for Na incorporation in garnet: an example from garnet in orthogneiss from the Su-Lu terrane, eastern China. Am. Mineral. 80, 475–482.
Fu, Y., Sun, X.M., Li, D.F., Lin, H., 2018. U-Pb geochronology and geochemistry of U-rich garnet from the giant Beiya gold-polymetallic deposit in SW China: constraints on skarn mineralization process. Minerals 8, 128.
Gaspar, M., Knaack, C., Meinert, L.D., Moretti, R., 2008. REE in skarn systems: a LA-ICP-MS study of garnets from the Crown Jewel gold deposit. Geochim. Cosmochim. Acta 72, 185–205.
Giuliani, G., Cheilletz, A., Mechiche, M., 1987. Behaviour of REE during thermal metamorphism and hydrothermal infiltration associated with skarn and vein-type tungsten ore bodies in central Morocco. Chem. Geol. 64, 279–294.
Grew, E.S., Marsh, J.H., Yates, M.G., Lazic, B., Armbruster, T., Locock, A., Bell, S.W., Dyar, M.D., Bernhardt, H.-J., Medenbach, O., 2010. Menzerite-(Y), a new species, {(Y, REE)(Ca, Fe2 +)2}[(Mg, Fe2 +) (Fe3 +, Al)] (Si3) O12, from a felsic granulite, Parry Sound, Ontario, and a new garnet end-member, {Y2Ca}[Mg2](Si3)O12. Can. Mineral. 48, 727–749.
Hou, Z.Q., Khin, Z., Qu, X.M., Ye, Q.T., Yu, J.J., Xu, M.J., Fu, D.M., Yin, X.K., 2001. Origin of the Gacun volcanic-hosted massive sulfide deposit in Sichuan, China: fluid inclusion and oxygen isotope evidence. Econ. Geol. 96, 1491–1512.
Jaffe, H.W., 1951. The role of yttrium and other minor elements in the garnet group. Am. Mineral. 36, 133–155.
Jamtveit, B., Ragnarsdottir, K.V., Wood, B.J., 1995. On the origin of zoned grossular-andradite garnets in hydrothermal systems. Eur. J. Mineral. 7, 1399–1410.
Jamtveit, B., Wogelius, R.A., Fraser, D.G., 1993. Zonation patterns of skarn garnets: Records of hydrothermal system evolution. Geology 21, 113–116.
Jollands, M.C., Hanger, B.J., Yaxley, G.M., Hermann, J., Kilburn, M.R., 2018. Timescales between mantle metasomatism and kimberlite ascent indicated by diffusion profiles in garnet crystals from peridotite xenoliths. Earth Planet. Sci. Lett. 481, 143–153.
Karimzadeh Somarin, A., 2004. Garnet composition as an indicator of Cu mineralization: Evidence from skarn deposits of NW Iran. J. Geochem. Explor. 81, 47–57.
Keankeo, W., Hermann, J., 2002. The oscillatory intergrowth of feldspars in titanian andradite, Little Dromedary, NSW. Australia. Eur. J. Mineral. 14, 379–388.
Kohn, M.J., 2004. Oscillatory- and sector-zoned garnets record cyclic (?) rapid thrusting in central Nepal. Geochem. Geophy. Geosy 5, 12.
Leng, C.B., 2017. Genesis of Hongshan Cu polymetallic large deposit in the Zhongdian area, NW Yunnan: constraints from LA-ICPMS trace element of pyrite and pyrrhotite. Geosci. Front. 24, 162–175 (in Chinese with English abstract).
Leng, C.B., Huang, Q.Y., Zhang, X.C., Wang, S.X., Zhong, H., Hu, R.Z., Bi, X.W., Zhu, J.J., Wang, X.S., 2014. Petrogenesis of the Late Triassic volcanic rocks in the Southern Yidun arc, SW China: constraints from the geochronology, geochemistry, and Sr–Nd–Pb–Hf isotopes. Lithos 190–191, 363–382.
Leng, C.B., Zhang, X.C., Hu, R.Z., Wang, S.X., Zhong, H., Wang, W.Q., Bi, X.W., 2012. Zircon U-Pb and molybdenite Re–Os geochronology and Sr–Nd–Pb–Hf isotopic constraints on the genesis of the Xuejiping porphyry copper deposit in Zhongdian, Northwest Yunnan. China. J. Asian Earth Sci. 60, 31–48.
Li, W.C., Wang, K.Q., Yin, G.H., Qin, D.H., Yu, H.J., Xue, S.R., Wan, D., 2013. Geochemical characteristics of ore-forming fluid and genesis of Hongshan copper deposit in northwest Yunnan Province. Acta Petrol. Sin. 29, 270–282 (in Chinese with English abstract).
Li, W.C., Yu, H.J., Gao, X., Liu, X.L., Wang, J.H., 2017. Review of Mesozoic multiple magmatism and porphyry Cu–Mo (W) mineralization in the Yidun Arc, eastern Tibet Plateau. Ore Geol. Rev. 90, 795–812.
Meinert, L.D., 1992. Skarns and skarn deposits. Geosci. Can. 19, 145–162.
Meng, J.Y., Yang, L.Q., Lü, L., Gao, X., Li, J.X., Luo, Y.Z., 2013. Re-Os dating of molybdenite from the Hongshan Cu-Mo deposit in Northwest Yunnan and its implications for mineralization. Acta Petrol. Sin. 29, 1214–1222 (in Chinese with English abstract).
Menzer, G., 1926. Die kristallstruktur von granat. Zeitschrift für Kristall. 63, 157–158.
Park, C., Choi, W., Kim, H., Park, M.H., Kang, I.M., Lee, H.S., Song, Y., 2017a. Oscillatory zoning in skarn garnet: Implications for tungsten ore exploration. Ore Geol. Rev. 89, 1006–1018.
Park, C., Song, Y., Kang, I.M., Shim, J., Chung, D., Park, C.S., 2017b. Metasomatic changes during periodic fluid flux recorded in grandite garnet from the Weondong W-skarn deposit, South Korea. Chem. Geol. 451, 135–153.
Peng, H.J., Li, H.Y., Pei, R.F., Zhang, C.Q., Zhou, Y.M., Tian, G., Li, J.X., Long, F., 2014a. Mineralogical characteristics and metallogeny of the Hongshan-Hongniu copper deposit in Zhongdian area, Yunnan province. China. Acta Petrol. Sin. 30, 237–256 (in Chinese with English abstract).
Peng, H.J., Mao, J.W., Pei, R.F., Zhang, C.Q., Tian, G., Zhou, Y.M., Li, J.X., Hou, L.,

2014b. Geochronology of the Hongniu-Hongshan porphyry and skarn Cu deposit, northwestern Yunnan province, China: Implications for mineralization of the Zhongdian arc. J. Asian Earth Sci. 79, 682–695.

Peng, H.J., Zhang, C.Q., Mao, J.W., Santosh, M., Zhou, Y.M., Hou, L., 2015. Garnets in porphyry–skarn systems: A LA–ICP–MS, fluid inclusion, and stable isotope study of garnets from the Hongniu-Hongshan copper deposit, Zhongdian area, NW Yunnan Province, China. J. Asian Earth Sci. 103, 229–251.

Pollok, K., Jamtveit, B., Putnis, A., 2001. Analytical transmission electron microscopy of oscillatory zoned grandite garnets. Contrib. Mineral. Petrol. 141, 358–366.

Qian, J.H., Wei, C.J., Zhou, X.W., Zhang, Y.H., 2013. Metamorphic P-T paths and new zircon U–Pb age data for garnet–mica schist from the Wutai Group, North China Craton. Precambr. Res. 233, 282–296.

Quartieri, S., Antonioli, G., Geiger, C.A., Artioli, G., Lottici, P.P., 1999a. XAFS characterization of the structural site of Yb in synthetic pyrope and grossular garnets. Phys. Chem. Miner. 26, 251–256.

Quartieri, S., Chaboy, J., Antonioli, G., Geiger, C.A., 1999b. XAFS characterization of the structural site of Yb in synthetic pyrope and grossular garnets. II: XANES full multiple scattering calculations at the Yb L_I- and L_{III}-edges. Phys. Chem. Miner. 27, 88–94.

Reid, A.J., Wilson, C.J.L., Liu, S., 2005a. Structural evidence for the Permo-Triassic tectonic evolution of the Yidun Arc, eastern Tibetan Plateau. J. Struct. Geol. 27, 119–137.

Reid, A.J., Wilson, C.J.L., Phillips, D., Liu, S., 2005b. Mesozoic cooling across the Yidun Arc, central-eastern Tibetan Plateau: a reconnaissance $^{40}Ar/^{39}Ar$ study. Tectonophysics 398, 45–66.

Shore, M., Fowler, A.D., 1996. Oscillatory zoning in minerals: A common phenomenon. Can. Mineral. 34, 1111–1126.

Shu, Q., Brey, G.P., Gerdes, A., Hoefer, H.E., 2013. Geochronological and geochemical constraints on the formation and evolution of the mantle underneath the Kaapvaal craton: Lu-Hf and Sm-Nd systematics of subcalcic garnets from highly depleted peridotites. Geochim. Cosmochim. Acta 113, 1–20.

Smit, M.A., Scherer, E.E., Mezger, K., 2013. Lu-Hf and Sm-Nd garnet geochronology: chronometric closure and implications for dating petrological processes. Earth Planet. Sci. Lett. 381, 222–233.

Smith, M.P., Henderson, P., Jeffries, T.E.R., Long, J., Williams, C.T., 2004. The rare earth elements and uranium in garnets from the Beinn an Dubhaich aureole, Skye, Scotland, UK: Constraints on processes in a dynamic hydrothermal system. J. Petrol. 45, 457–484.

Spengler, D., Obata, M., Hirajima, T., Ottolini, L., Ohfuji, H., Tamura, A., Arai, S., 2012. Exsolution of garnet and clinopyroxene from high-Al pyroxenes in Xugou Peridotite, Eastern China. J. Petrol. 53, 1477–1504.

Sun, C.G., Liang, Y., 2015. A REE-in-garnet–clinopyroxene thermobarometer for eclogites, granulites and garnet peridotites. Chem. Geol. 393–394, 79–92.

Sun, S.S., Mcdonough, W.F., 1989. Chemical and isotopic systematics of oceanic basalts: implications for mantle composition and processes. Geol. Soc. London Spec. Publ. 42, 313–345.

Vander Auwera, J., Andre, L., 1991. Trace elements (REE) and isotopes (O, C, Sr) to characterize the metasomatic fluid sources: evidence from the skarn deposit (Fe, W, Cu) of Traversella (Ivrea, Italy). Contrib. Mineral. Petrol. 106, 325–339.

Wang, B.Q., Zhou, M.F., Li, J.W., Yan, D.P., 2011a. Late Triassic porphyritic intrusions and associated volcanic rocks from the Shangri-La region, Yidun terrane, Eastern Tibetan Plateau: Adakitic magmatism and porphyry copper mineralization. Lithos 127, 24–38.

Wang, P., Dong, G.C., Li, X.F., Chen, W., Li, J.X., Tao, X.X., 2017a. Metallogenic sources of the Hongshan-Hongniu copper deposit in northwestern Yunnan: constraints from mineralogy and stable isotope. Geosci. Front. 24, 176–193 (in Chinese with English abstract).

Wang, P., Dong, G.C., Santosh, M., Liu, K.R., Li, X.F., 2017b. Copper isotopes isotopes trace the evolution of skarn ores: a case study from the Hongshan-Hongniu Cu

deposit, southwest China. Ore Geol. Rev. 88, 822–831.

Wang, X.S., Bi, X.W., Leng, C.B., Tang, Y.Y., Lan, J.B., Qi, Y.Q., Shen, N.P., 2011b. LA-ICP-MS zircon U-Pb dating of granite porphyry in the Hongshan Cu-polymetallic deposit, Zhongdian, Northwest Yunnan, China and its geological implications. Acta Mineral. Sin. 31, 315–321 (in Chinese with English abstract).

Wang, X.S., Bi, X.W., Leng, C.B., Zhong, H., Tang, H.F., Chen, Y.W., Yin, G.H., Huang, D.Z., Zhou, M.F., 2014. Geochronology and geochemistry of Late Cretaceous igneous intrusions and Mo–Cu–(W) mineralization in the southern Yidun Arc, SW China: implications for metallogenesis and geodynamic setting. Ore Geol. Rev. 61, 73–95.

Wang, Y.F., Merino, E., 1992. Dynamic model of oscillatory zoning of trace elements in calcite: Double layer, inhibition, and self-organization. Geochim. Cosmochim. Acta 56, 587–596.

Wood, B.J., Kiseeva, E.S., Matzen, A.K., 2013. Garnet in the earth's mantle. Elements 9, 421–426.

Wu, T., Xiao, L., Wilde, S.A., Ma, C.Q., Zhou, J.X., 2017. A mixed source for the Late Triassic Garzê-Daocheng granitic belt and its implications for the tectonic evolution of the Yidun arc belt, eastern Tibetan Plateau. Lithos 288–289, 214–230.

Xiao, X., Zhou, T.F., White, N.C., Zhang, L.J., Fan, Y., Wang, F.Y., Chen, X.F., 2018. The formation and trace elements of garnet in the skarn zone from the Xinqiao Cu-S-Fe-Au deposit, Tongling ore district, Anhui Province, Eastern China. Lithos 302–303, 467–479.

Xu, J., Ciobanu, C.L., Cook, N.J., Zheng, Y.Y., Sun, X., Wade, B.P., 2016. Skarn formation and trace elements in garnet and associated minerals from Zhibula copper deposit, Gangdese Belt, southern Tibet. Lithos 262, 213–231.

Xu, L.J., Xiao, Y.L., Wu, F., Li, S.G., Simon, K., Worner, G., 2013. Anatomy of garnets in a Jurassic granite from the south-eastern margin of the North China Craton: magma sources and tectonic implications. J. Asian Earth Sci. 78, 198–221.

Xu, X.W., Cai, X.P., Qu, W.J., Song, B.C., Qin, K.Z., Zhang, B.L., 2006. Late Cretaceous granite porphyritic Cu-Mo mineralization system in the Hongshan area, Northwestern Yunnan and its significances for tectonics. Acta Geol. Sin. 80, 1422–1433 (in Chinese with English abstract).

Yang, L.Q., Gao, X., Shu, Q.H., 2017. Multiple Mesozoic porphyry-skarn Cu (Mo–W) systems in Yidun terrane, east Tethys: constraints from zircon U-Pb and molybdenite Re–Os geochronology. Ore Geol. Rev. 90, 813–826.

Yardley, B.W.D., Rochelle, C.A., Barnicoat, A.C., Lloyd, G.E., 1991. Oscillatory zoning in metamorphic minerals: an indicator of infiltration metasomatism. Mineral. Mag. 55, 357–365.

Zhai, D.G., Liu, J.J., Zhang, H.Y., Wang, J.P., Su, L., Yang, X.A., Wu, S.H., 2014. Origin of oscillatory zoned garnets from the Xieertala Fe–Zn skarn deposit, northern China: In situ LA–ICP-MS evidence. Lithos 190–191, 279–291.

Zhang, Y., Liu, Q.Q., Shao, Y.J., Li, H.B., 2017a. Fingerprinting the hydrothermal fluid characteristics from LA-ICP-MS trace element geochemistry of garnet in the Yongping Cu deposit, SE China. Minerals 7, 199.

Zhang, Y., Shao, Y.J., Wu, C.D., Chen, H.Y., 2017b. LA-ICP-MS trace element geochemistry of garnets: Constraints on hydrothermal fluid evolution and genesis of the Xinqiao Cu–S–Fe–Au deposit, eastern China. Ore Geol. Rev. 86, 426–439.

Zhou, J.H., Feng, C.Y., Li, D.X., 2017. Geochemistry of the garnets in the Baiganhu W-Sn orefield, NW China. . Ore Geol. Rev. 82, 70–92.

Zu, B., Xue, C.J., Chi, G.X., Zhao, X.B., Li, C., Zhao, Y., Yalikun, Y., Zhang, G.Z., Zhao, Y., 2016. Geology, geochronology and geochemistry of granitic intrusions and the related ores at the Hongshan Cu-polymetallic deposit: Insights into the Late Cretaceous post-collisional porphyry-related mineralization systems in the southern Yidun arc, SW China. Ore Geol. Rev. 77, 25–42.

Zu, B., Xue, C.J., Zhao, Y., Qu, W.J., Li, C., Symons, D.T.A., Du, A.D., 2015. Late Cretaceous metallogeny in the Zhongdian area: Constraints from Re–Os dating of molybdenite and pyrrhotite from the Hongshan Cu deposit, Yunnan, China. Ore Geol. Rev. 64, 1–12.